The 2019 Southern Hemisphere stratospheric polar vortex weakening and its impacts

Eun-Pa Lim[1], Harry H. Hendon[1], Amy H. Butler[2], David W. J. Thompson[3], Zachary Lawrence[4], Adam A. Scaife[5,6], Theodore G. Shepherd[7], Inna Polichtchouk[8], Hisashi Nakamura[9], Chiaki Kobayashi[10], Ruth Comer[5], Lawrence Coy[11,12], Andrew Dowdy[1], Rene D. Garreaud[13], Paul A. Newman[11], and Guomin Wang[1].

[1] Bureau of Meteorology, Melbourne, Australia

[2] NOAA Chemical Sciences Laboratory, Boulder, Colorado, USA

[3] Department of Atmospheric Science, Colorado State University, Fort Collins, Colorado, USA

[4] NOAA Physical Sciences Laboratory, Boulder, Colorado, USA

[5] Met Office Hadley Centre, Exeter, UK

[6] College of Engineering, Mathematics and Physical Sciences, University of Exeter, UK

[7] Department of Meteorology, University of Reading, Reading, UK

[8] European Centre for Medium-Range Weather Forecasts, Reading, UK

[9] Research Center for Advanced Science and Technology, University of Tokyo, Japan

[10] Meteorological Research Institute, Japan Meteorological Agency, Tsukuba, Japan

[11] NASA Goddard Space Flight Center, Greenbelt, Maryland, USA

[12] Science Systems and Applications, Inc., Lanham, Maryland, USA

[13] Department of Geophysics, University of Chile, Chile

Corresponding author: eun-pa.lim@bom.gov.au

Capsule Summary

During austral spring 2019 the Antarctic stratosphere experienced record-breaking warming and a near-record polar vortex weakening, resulting in predictable extreme climate conditions throughout the Southern Hemisphere through December 2019.

Abstract

This study offers an overview of the low-frequency (i.e., monthly to seasonal) evolution, dynamics, predictability, and surface impacts of a rare Southern Hemisphere (SH) stratospheric warming that occurred in austral spring 2019. Between late August to mid-September 2019, the stratospheric circumpolar westerly jet weakened rapidly, and Antarctic stratospheric temperatures rose dramatically. The deceleration of the vortex at 10 hPa was as drastic as that of the first ever observed major sudden stratospheric warming in the SH during 2002, while the mean Antarctic warming over the course of spring 2019 broke the previous record of 2002 by ~50% in the mid-stratosphere. This event was preceded by a poleward shift of the SH polar night jet in the uppermost stratosphere in early winter, which was then followed by record-strong planetary wave-one activity propagating upward from the troposphere in August that acted to dramatically weaken the polar vortex throughout the depth of the stratosphere. The weakened vortex winds and elevated temperatures moved downward to the surface from mid-October to December, promoting a record strong swing of the Southern Annular Mode (SAM) to its negative phase. This record-negative SAM appeared to be a primary driver of the extreme hot and dry conditions over subtropical eastern Australia that accompanied the severe wildfires that occurred in late spring 2019. State-of-the-art dynamical seasonal forecast systems skilfully predicted the significant vortex weakening of spring 2019 and subsequent development of negative SAM from as early as late July.

Introduction

Sudden stratospheric warming events (SSWs) are characterized by dramatic warming and weakening of the stratospheric polar vortex. SSWs have a profound impact on stratospheric circulation and chemical composition and can drive sustained anomalies in surface weather, altering the occurrence of weather and climate extremes (e.g., Kidston et al. 2015; King et al. 2019; Lim et al. 2019), thus serving as an important source of long-range predictability (e.g., Baldwin and Dunkerton 2001; Domeisen et al. 2020). Major SSWs, which are defined by a reversal of the climatological westerly vortex in the mid-stratosphere followed by a recovery (Charlton and Polvani 2007; Butler et al. 2015), occur every 1-2 years on average in the Northern Hemisphere (NH), but are extremely rare in the Southern Hemisphere (SH): only one major SSW has been observed in the SH over the past ~60 years, which occurred during late September 2002 (e.g., Baldwin et al. 2003; Dowdy et al. 2004; Nishii and Nakamura 2004; Shepherd et al. 2005).

The 2002 major SSW, which was a vortex-splitting event, occurred with extraordinarily strong wave forcing from the troposphere throughout the preceding austral winter and the associated contraction of the polar vortex from late winter (e.g., Harnik et al. 2005; Newman and Nash 2005; Scaife et al. 2005). It then dramatically developed over 10 days from 17 September with upper stratospheric preconditioning (e.g., Newman and Nash 2005; Scaife et al. 2005) and resonant amplification of wave forcing within the stratosphere (Esler et al. 2006), and the wind reversal occurred during 25-30 September. During the 2002 SSW, the stratospheric jet at 10 hPa weakened by 80 ms^{-1} and the Antarctic polar cap (the area mean over 60-90°S) warmed by 32 K at 30 hPa from September 17 to 27 (NASA Ozone Watch; https://ozonewatch.gsfc.nasa.gov/). These extreme wind and temperature anomalies subsequently coupled downward, leading to the record strong low polarity (negative) index of

72 the Southern Annular Mode (SAM; Thompson and Wallace 2000) and associated surface
73 climate extremes in the following spring months (Thompson et al. 2005; Hendon et al. 2020).

74 Beginning in late August 2019, the SH stratospheric polar vortex experienced radical
75 warming and weakening, which was of comparable magnitude to what occurred during 2002,
76 and was displaced from the South Pole (rather than split). Lim et al. (2020) and subsequent
77 studies (e.g., Eswaraiah et al. 2020; Rao et al. 2020; Shen et al. 2020) reported that the
78 stratospheric jet at 10 hPa at 60°S weakened by 80 ms^{-1}, and the polar cap warmed by 35 K at
79 30 hPa during the three weeks following 25 August 2019, setting records for the highest polar
80 cap temperature and weakest westerly jet in the mid to upper stratosphere in September.

81 The weakened vortex in September then coupled downward to the troposphere from
82 mid-October to December 2019, with an extraordinarily persistent equatorward shift of the
83 tropospheric eddy-driven westerly jet and a concomitant increase of surface pressure in the
84 polar region and a decrease in the SH midlatitudes. Together these changes characterize a
85 swing to the negative phase of the SAM (hereafter, referred to as negative SAM), which
86 typically follows anomalous springtime weakening of the SH polar vortex, such as those
87 observed in 1988 and 2002 (Thompson et al. 2005; Seviour et al. 2014; Byrne and Shepherd
88 2018; Lim et al. 2019). The negative SAM in late spring 2019 was record-strong for the
89 season and played a significant role in exacerbating the pre-existing hot and dry conditions
90 over Australia, which were conducive to the devastating wildfires (known as bushfires in
91 Australia) that ensued along the central east coast (Phillips and Nogrady 2020). It also
92 contributed to below-average rainfall in northeastern Brazil and eastern South Africa, and
93 above-average rainfall in southeastern Brazil, western Patagonia and southernmost New
94 Zealand during late October through December 2019 (Lim et al. 2020).

95 Recent studies have already unraveled some key mechanisms that triggered the SSW
96 in mid-September 2019 on daily to weekly timescales (Eswaraiah et al. 2020; Rao et al. 2020;

97 Shen et al. 2020) and have identified significant impacts of this event on the different
98 atmospheric layers and regions (Yamazaki et al. 2020; Noguchi et al. 2020; Anstey et al.
99 2020; Wargan et al. 2020). Here we concentrate on the low-frequency (i.e., spring season)
100 manifestation of the 2019 SSW, which is, hereafter, referred to as springtime stratospheric
101 polar vortex (SPV) weakening. We show that the origin of this event can be traced back to
102 changes in the polar night jet (PNJ) at the stratopause as early as June 2019 and whose
103 surface impacts were felt through December 2019. We also explore the long-lead
104 predictability of the springtime SPV weakening event using both inferences from lagged
105 statistical relationships based on historical data and coupled model seasonal forecast systems
106 (as opposed to a deterministic prediction of the precise timing of the SSW) and of the
107 sustained surface impacts into austral late spring/early summer 2019. This focus on the
108 monthly to seasonal timescale evolution of the stratospheric circulation associated with the
109 vortex weakening event and its sustained coupling downward to the surface highlights that
110 springtime SPV variability and associated preconditioning processes are a potential source of
111 predictability of surface climate with lead times much longer than associated with predction
112 of the abrupt SSW.

113 For the observational analysis, we have used the Japanese Reanalysis-55 dataset
114 (JRA-55; Kobayashi et al. 2015) and Global Precipitation Climatology Project (GPCP)
115 precipitation version 2.3 dataset (Adler et al. 2018) for 1979-2019. We computed anomalies
116 for 2019 using the climatology of 1979-2018. For the SPV index and other climate indices,
117 we normalized the index anomalies by their standard deviations (σ) obtained from the
118 climatological 40 year data. We also analyzed the Australian Water Availability Project
119 (AWAP) gridded analyses (Jones et al. 2009) of Australian temperature and rainfall and a

120 gridded dataset of the McArthur forest fire danger index[1] (Dowdy 2018) to examine the
121 impact of the 2019 SPV weakening on Australian climate in late 2019.

122 The coupled model seasonal hindcasts for 1990-2012 and real-time forecasts for 2019
123 were produced from the operational systems of the Australian Bureau of Meteorology (BoM
124 ACCESS-S1; Hudson et al. 2017), the European Centre for Medium-Range Weather
125 Forecasts (ECMWF-SEAS5; Johnson et al. 2018), the Japan Meteorological Agency
126 (JMA/MRI-CPS2; Takaya et al. 2018), NASA (GEOS-S2S-2; Molod et al. 2020), and the
127 UK Met Office (UKMO GloSea5; MacLachlan et al. 2015). Details of the forecast sytems
128 and configurations are described in Table 1.

129 Setting new records

130 The PNJ, the Antarctic temperatures, and the SAM were all severely disrupted in association
131 with the 2019 SPV weakening. Figure 1a shows Antarctic circumpolar zonal wind anomalies
132 at 60°S (shading) for 1 June to 31 December 2019 (1000 hPa to 1 hPa) superimposed on the
133 climatology (contours). The sudden and massive vortex weakening in the upper stratosphere
134 began in late August and then extended downward into the troposphere from October through
135 the end of December, manifested as persistent period of strong negative SAM (Fig. 1b),
136 which is monitored with the CPC AAO index (available at
137 https://www.cpc.ncep.noaa.gov/products/precip/CWlink/daily_ao_index/aao/aao.shtml;

[1] The McArthur Forest Fire Danger Index (FFDI) was obtained from a dataset as described by Dowdy (2018), based on a gridded analysis of observations at 0.05 degrees in both latitude and longitude throughout Australia. The FFDI is calculated as an exponential function combining relative humidity, temperature and wind speed as well as a drought factor based on a measure of fuel dryness calculated from antecedent rainfall and temperature. The FFDI has been shown to exhibit predictability on seasonal timescales (Bett et al. 2020), but it is used here as a useful way of combining various weather factors known to influence fire danger and for providing broad-scale guidance on climatological features including its relationship to large-scale atmospheric and oceanic modes of variability such as the SAM, stratospheric polar vortex and El Nino-Southern Oscillation.

Thompson and Wallace 2000). Concomitant with the vortex weakening, the polar cap temperature rapidly increased in the upper to mid stratosphere and then stayed significantly warmer than normal in the lower stratosphere through December (Fig. 1c). Consistent with thermal-wind balance, the maximum warm anomalies sit below the maximum easterly anomalies. By comparing to the climatological zonal wind, the springtime SPV weakening of 2019 can be viewed as an accelerated march of the seasonal cycle of the SH stratospheric circulation, resulting in an earlier-than-normal breakdown of the winter vortex (e.g., Shiotani et al. 1993; Taguchi and Yoden 2002; Hio and Yoden 2005; Byrne and Shepherd 2018).

Although the 2019 SSW did not experience a zonal wind reversal at 60°S and 10 hPa to qualify as a major SSW (e.g., Butler et al. 2015), many other measures point to this event being of record strength, especially when viewed on longer (monthly to seasonal) timescales. For example, the austral springtime mean (September-November; SON) zonal-mean zonal wind ([U]) at 60°S and 1 hPa was the weakest on record by a big margin over the previous records (-3σ compared to -2σ in 1988 and 2002) (e.g., Eswaraiah et al. 2020); and the weakening of [U] at 60°S and 10 hPa was on a par with 2002, with a magnitude of -3.0σ (Fig. 2b). Similarly, the amplitude of the leading empirical orthogonal function (EOF) of Antarctic polar cap geopotential height anomalies at 30 hPa, which depicts the earlier/later breakdown of the SH stratospheric polar vortex (Byrne and Shepherd 2018), was 2.3σ in both 2002 and 2019 (Supplementary Figs. S1a,b). Likewise, the leading time-height EOF of Antarctic circumpolar zonal wind, which also captures the variability of the canonical life cycle of the SH stratospheric vortex weakening and its downward coupling to the troposphere that typically evolves from early winter at the stratopause to summer at the surface (Lim et al. 2018), exhibited the record magnitude of 2.5σ in 2002 and 2019 (Supplementary Figs. S1c,d).

There were two records related to the SPV weakening: springtime polar stratospheric temperatures and ozone concentrations were both at record highs – resulting in a very small

Antarctic ozone hole. The record high temperatures were especially evident in the mid-stratosphere (30 hPa) where the polar temperature anomaly was about 50% higher than in 2002 (Fig. 2c). Typically, Antarctic polar cap ozone increases as the SH stratospheric polar vortex weakens and warms (e.g., Stolarski et al. 2005; Keeble et al. 2014; Seviour et al. 2014). The strengthened Brewer-Dobson circulation associated with the 2019 SPV weakening (Noguchi et al. 2020) transported mid-stratospheric ozone from the midlatitudes into the polar region, while also developing an enhanced downward circulation that warmed the polar lower stratosphere (Wargan et al. 2020). This warming curtailed the typical chlorine and bromine catalytic ozone loss processes that cause the ozone hole. The polar cap total column ozone concentration in SON 2019 was the highest on record since 1979 (Fig. 2d) primarily due to the SPV weakening (Wargan et al. 2020).

Despite the extraordinarily early start of the 2019 SSW in late August, the wind and temperature anomalies did not couple down to the troposphere until mid-October. However, once the stratosphere-troposphere coupling occurred, the resultant SAM index averaged over October-December was the most strongly negative on record for that season (Fig. 2e), which is consistent with a strong correlation between the October-December SAM index (Fig. 2c) and the springtime SPV index (SPVI; defined here as [U] at 60°S and 10 hPa averaged for the SON season (Seviour et al. 2014); Fig. 2b) over 1979-2018 (r ~0.66).

Dynamical processes for the 2019 stratospheric vortex weakening

Before the drastic weakening of the polar vortex in September 2019, the PNJ at the stratopause first shifted poleward during early austral winter (June-July), which is likely due to increased wave forcing in early winter (e.g. Kodera and Kuroda 2002). The evolution of the 2019 vortex weakening and a comparison to historically observed SH springtime SPV events are shown in Figure 3. The right-hand column displays the 2019 evolution of zonal-mean zonal wind anomalies ([U]') at 1 hPa (near the stratopause), 10 hPa (mid-stratosphere)

188 and 100 hPa (lower stratosphere) as a function of calendar month. The left-hand column
189 displays the same fields but derived from the regression onto the SPVI displayed in Fig. 2b.
190 The regression coefficient patterns were obtained using data for the period 1979-2018, and
191 the syntheses for 2019 were obtained by multiplying the regression coefficients by the 2019
192 value of the SPVI to show the evolution of [U]' at these different levels that was expected
193 from the 2019 SPV weakening in spring (see details in Supplemental Material).

194 For both the synthesized and observed anomalies of 2019, the development of easterly
195 anomalies in the mid and lower stratospheric polar vortex from September onward can be
196 traced back to a poleward shift (i.e., a meridional dipole anomaly) of the PNJ at 1 hPa during
197 early winter (Figs. 3a,b). This meridional dipole anomaly in the upper stratospheric westerlies
198 peaks in July and then gradually moves poleward through August in conjunction with the
199 seasonal poleward shift of the jet from winter to spring (e.g., Kodera and Kuroda 2002; Byrne
200 and Shepherd 2018). Beginning in September, the upper stratospheric wind anomaly takes the
201 form of a monopole weakening of the vortex that extends from 30°S to the pole. This rapid
202 latitudinal expansion of the easterly anomalies in the upper stratosphere in September,
203 reflecting the sustained effects of a weakened vortex, concurs with the appearance of easterly
204 anomalies in the mid to lower stratosphere that then persist through at least December (Figs.
205 3c-f).

206 We note that springtime weakening of the SH polar vortex coincides with easterly
207 anomalies in the low latitudes equatorward of 10°S at 10 hPa in both the canonical
208 development derived from regression and in the 2019 anomalies (Figs. 3c,d). The tropical
209 easterly anomalies at 10 hPa are a signal accompanying the westerly phase of the quasi-
210 biennial oscillation (QBO) defined at 30-50 hPa (e.g., Anstey et al. 2010; Shen et al. 2020;
211 for the QBO in 2019, see https://acd-ext.gsfc.nasa.gov/Data_services/met/qbo/qbo.html).
212 Tropical stratospheric winds could potentially alter wave propagation characteristics and/or

213 the stratospheric residual mean circulation in ways that affect thepolar vortex (Holton and
214 Tan 1980; Baldwin et al. 2001; Anstey and Shepherd 2014; Byrne and Shepherd 2018; Gray
215 et al. 2020). Given the statistically significant connection between the easterly signal of the
216 QBO in May and a poleward shift of the westerly jet in the subsequent winter months at 10
217 hPa (Fig. 3c), an in-depth investigation is warranted for the influence of the QBO related
218 mid-stratospheric easterlies on the different stages of the polare vortex evolution during 2019
219 although Shen et al. (2020) briefly noted that the tropical easterly anomalies at 10 hPa
220 associated with the QBO were unlikely to be a direct cause of the 2019 SSW. On the other
221 hand, Anstey et al. (2020) suggest that the 2019 SSW impacted the QBO and its
222 predictability by significantly distrupting the downward propagation of the tropical easterly
223 anomalies to the lower stratosphere.

224 The preceding poleward shift of the PNJ during austral winter for both the historical
225 development of springtime vortex weakening and the 2019 event is maintained by a similar
226 dipole pattern of anomalous meridional eddy momentum flux convergence in the upper
227 stratosphere (Figs. 4a,b). Anomalous upward flux of wave activity from the troposphere into
228 the stratosphere, as indicated by the poleward eddy heat flux[2] at 100 hPa, develops over 50°-
229 70°S from July and peaks in September (Matsuno 1970; Shiotani et al. 1993; Kuroda and
230 Kodera 1998; Newman et al. 2001; Hio and Yoden 2005) (Figs. 4c,d).

231 The increased westerlies at 1 hPa (Fig. 3a) and associated increased upward and
232 equatorward propagating wave activities in the lower and upper stratosphere, respectively
233 (Figs. 4c and 4a), all appear on the poleward sides of their climatological maxima during July
234 and August. This is consistent with the concept that poleward movement of the winter PNJ,
235 which happens when Rossby waves break in the subtropical surf zone, acting to sharpen the

[2] The poleward eddy heat flux represents the upward flux of wave activity (Newman and Nash 2005). The poleward heat flux is negatively signed in the SH (i.e., northward heat flux being positive).

potential vorticity gradient and causing the polar vortex to shrink towards the pole, may focus upward propagating wave activity into the polar cap, subsequently acting to weaken the vortex (McIntyre and Palmer 1983; Kodera and Kuroda 2002; Harnik et al. 2005; Albers and Birner 2014; Lawrence and Manney 2020 and references therein). The poleward heat flux anomalies at 100 hPa increase dramatically from July to October (Fig. 4c), and the convergence of this heat flux in the vertical exerts the necessary easterly forcing to weaken the vortex from August onward (Supplementary Fig. S2). The 2019 anomalies appear to closely follow the canonical evolution of the upper stratospheric winds and planetary wave activity for springtime polar vortex weakening, but the poleward heat flux anomalies at 100 hPa were extraordinarily strong in August and September 2019 (Fig. 4d), which was consistent with the resultant record weakening of the polar vortex.

More details of the increased poleward heat flux during 2019 are provided in Figure 5a, which displays the standardized amplitudes of the wave-1 poleward heat flux anomalies averaged over 45-75°S at different vertical levels during May-December 2019 (Jucker 2016; Birner and Albers 2017). We limit our interest to the wave-1 heat flux as it was the most dominant component in the wave forcing for the 2019 SSW (Rao et al. 2020; Shen et al. 2020), although there was a substantial positive contribution of the wave-2 heat flux in July (Supplementary Fig. S3). The initial wave-1 poleward heat flux increases in June were confined to the mid and upper stratosphere, consistent with the poleward contraction of the PNJ as discussed earlier. Subsequently in August and September 2019, extraordinarily strong heat flux anomalies ($< -3\sigma$) developed throughout the troposphere and stratosphere (e.g., Milinevsky et al. 2019). This wave-1 heat flux event of August 2019 was the 2nd strongest in the lower troposphere (after 1988) and the strongest at 100 hPa since 1979 (Supplementary Fig. S4).

Although a growing body of research shows that SSWs can occur without the anomalous upward wave activity flux emanating from the troposphere (e.g., Scott and Polvani 2004; Esler and Scott 2005; Jucker 2016; Birner and Albers 2017), an indication of the tropospheric source of the enhanced upward injection of wave activity (i.e., enhanced poleward heat flux) in late winter 2019 is provided by the August-mean eddy geopotential height averaged over 45-75°S (Fig. 5b) and 700 hPa geopotential height anomalies (Z700) (Fig. 5c). The observed SH Z700 anomalies in August 2019 are characterized by a primary anticyclonic anomaly over the Bellingshausen-Amundsen Seas and a secondary anticyclonic anomaly in the Southern Indian Ocean south of Australia with two cyclonic anomaly centers in-between. This pattern strongly projects onto the Z700 anomaly patterns associated with the increase of the wave-1 poleward heat flux at 700 hPa and, to a less degree, at 100 hPa (Supplementary Fig. S5). The eddy geopotential height pattern of 2019 shows that this lower tropospheric wave pattern propagates upward with a westward tilt, significantly amplifying in the upper stratosphere (Fig. 5b), suggesting that the anomalous tropospheric wave pattern in 2019 was conducive to vertical wave propagation. Rao et al. (2020) and Shen et al. (2020) show that the upward propagating wave-1 activity further increased in September, playing a key role in the onset of the SSW.

Our preliminary investiagtion to find possible sources of this extraordinary increase of the wave-1 poleward heat flux hints that convection anomalies over the tropical-subtropical Indian and western Pacific Oceans could have acted as the sources of the teleconnection that promoted the August lower tropospheric circulation anomaly (Supplementary Fig. S6). More sophisticated wave analysis and/or carefully designed dynamical modelling experiments would help further elucidate possible tropical influences on the poleward heat fluxes and resultant SH spring vortex variations, which is beyond the scope of this study.

Impact on the SH regional climate

The 2019 stratospheric vortex weakening signal descended to the surface from mid-October through December (Fig. 1), setting a new record for negative SAM for that season (Fig. 2e). Negative SAM is characterized by equatorward shifts of the tropospheric eddy-driven westerly jet and associated midlatitude storm track, therefore bringing wet and cold conditions to western Patagonia and southeast South America (SA), western Tasmania, and southern New Zealand and dry westerly winds over southern portions of Australia in the October to December season (OND) as well as in austral summer (e.g., Gillett et al. 2006; Lim et al. 2018; Garreaud 2018). Additionally, negative SAM is accompanied by an equatorward shift of the descending branch of the SH Hadley cell in austral warm seasons (e.g,. Kang et al. 2011; Ceppi and Hartmann 2013; Hendon et al. 2014), therefore resulting in increased downward motion and reduced cloudiness in the SH subtropics and associated dry and warm conditions, which are most prominent over eastern Australia (Lim et al. 2018, 2019).

The SH horizontal and vertical circulation anomalies of OND 2019 closely followed the canonical responses to the springtime SPV weakening, as depicted by regression onto the SPVI (Fig. 6). Although the observed pressure anomalies depict negative SAM (Fig. 6b), they are less zonally symmetric than the canonical response to vortex weakeing especially over the central and eastern portions of the South Pacific (Fig. 6a). This feature is largely explained by the presence of Central Pacific (CP) El Nino and the extraordinarily strong positive Indian Ocean dipole mode (IOD) (Supplementary Figs. S7a-c), which are monitored

by the El Nino Modoki Index (EMI[3]; Ashok et al. 2007) and the Dipole Mode Index (DMI[4]; Saji et al. 1999) (Supplementary Fig. S8), respectively. Both CP El Nino and IOD promote Rossby wave trains that propagate toward the southeast Pacific, thereby contributing to zonally asymmetric circulations in the SH extratropics (Supplementary Figs. S7d-f; e.g., Ashok et al. 2007; Cai et al. 2011). Consequently, the large-scale circulation anomalies over the southern Atlantic and far eastern Pacific were weaker than those typically observed during the springtime SPV weakening and negative SAM, which led to only moderate wet anomalies in western Patagonia and cold anomalies in the southern tip of SA and around the Antarctic Peninsula (Fig. 6 right panels). In contrast, a dipole of precipitation and temperature anomalies along eastern SA was prominent in late spring 2019: eastern Brazil was significantly warmer and drier than normal with significantly enhanced downward motion and reduced cloud cover, whereas the opposite conditions occurred in Uruguay and parts of Argentina (Fig. 6d, Supplementary Fig. S9b). These dipole patterns are similar to those associated with the springtime SPV weakening and negative SAM (Fig. 6c, Supplementary Fig. S9a) but much more intense.

As broadcast world-wide, eastern Australia suffered from extreme hot and dry conditions and resultant severe wildfires during OND 2019 (e.g., Phillips and Nogrady 2020). Significantly enhanced downward motion, clearer skies, higher temperatures, and lower rainfall over eastern Australia were highly consistent with the anomalies expected to occur during SPV weakening and negative SAM (Fig. 6 and Supplementary Fig. S9; Lim et al. 2019). Furthermore, the positive IOD in OND 2019 was record strong for the season as

[3] $EMI = \overline{SST}cp - 0.5 * (\overline{SST}ep + \overline{SST}\,wp)$, where cp denotes tropical central Pacific (10°S-10°N, 165-220°E), ep denotes tropical eastern Pacific (15°S-5°N, 250-290°E), and wp denotes tropical western Pacific (10°S-20°N, 125-145°E). The overbar represents the area average.

[4] $DMI = \overline{SST}(10°S - 10°N, 50 - 70°E) - \overline{SST}(0 - 10°S, 90 - 110°E)$ where the overbar denotes the area average.

326 evidenced by the DMI being greater than 3σ, and CP El Nino was strong as well, as judged
327 by the EMI being 1σ in NOAA OI v2 SST data (Reynolds et al. 2002) (which was combined
328 with Hurrell et al. (2008) SST data for 1979-1981 in our analysis) (Supplementary Fig. S8).
329 These anomalous SST conditions are well-known drivers of hot and dry conditions over
330 Australia in its spring season (e.g., Saji and Yamagata 2003; Wang and Hendon 2007; Cai et
331 al. 2011), providing long-lead predictability. All these extreme large-scale conditions
332 impacted Australian late spring climate on top of its on-going long-term warming trend,
333 much of which is thought to be anthropogenically driven (Reisinger et al. 2014), and the
334 multi-year drought that had begun in 2017
335 (http://www.bom.gov.au/climate/drought/knowledge-centre/previous-droughts.shtml).
336 Together, they resulted in extreme conditions for wildfire occurrence across the country.

337 To better understand the relative roles of the stratospheric polar vortex weakening
338 (and associated negative SAM), CP El Nino, the positive IOD, and the linear long-term trend
339 for the late spring extreme climate of Australia in 2019, we have synthesized the Australian
340 daily maximum temperature (Tmax), rainfall, and forest fire danger index (FFDI) for late
341 spring (OND) 2019, based on multiple linear regression. For this "storyline" approach
342 (Shepherd 2019), we used four predictors – the de-trended EMI and DMI for OND, the de-
343 trended SPVI, and time to capture any trend since 1979[5]. Figure 7 shows that all four
344 predictors significantly contributed to the hot, dry, and fire-prone conditions over different
345 parts of Australia. CP El Nino contributed to drier conditions country-wide but especially in
346 the north (Figs. 7a,g,m) while the positive IOD contributed to intense hot, dry, and dangerous
347 fire weather conditions in the southeast (Figs. 7b,h,n). The linear trend since 1979 contributed

[5] The EMI and DMI of the October-December mean and the SPVI of Septemper-November mean do not have any significant trends over the study period 1979-2018, and they are not significantly correlated to one another ($p > 0.1$).

more modestly to the warming in the southern half of the country while making the northwest wetter (Figs. 7d,j,p). The springtime SPV weakening and associated negative SAM appears to have played the most prominent role in the hot, dry, and fire-conducive weather conditions in subtropical eastern Australia (Figs. 7c,i,o), especially along the eastern seaboard of southern Queensland and New South Wales, where severe wildfires occurred from October to December[6]. For the FFDI averaged east of 150°E (the dashed vertical line in Figs. 7m-r), the SPV weakening contributed 43% (28%) to the reconstructed (observed) anomaly, while CP El Nino, the positive IOD and the linear trend contributed 21%, 24%, and 12% (14%, 16%, and 8%) to the reconstruction (observation), respectively.

Although the reconstructed Tmax, rainfall, and fire danger index reasonably well capture the observed conditions in the east (Fig. 7 right two columns), the hot and dry and forest fire danger anomalies in the north and the west of the country far exceeded the reconstruction based on these four large-scale oceanic and atmospheric drivers over the last 40 year period. It is important to note that apart from the linear trend shown in Fig. 7, it is challenging to disentangle more complicated potential influences of multi-year to decadal variabilities and climate change on the Australian climate extremes and wildfire risks observed in late spring 2019, which require data of longer records and/or carefully designed dynamical model experiments. Despite this inherent limitation of our simple statistical analysis method, it still provides valuable insight that more than half of the observed forest fire danger risk over the fire-struck region in the southeast could be explained by the internally-driven dynamical circulation anomalies, and about half of that circulation-driven risk could be explained by the record strong stratospheric warming event.

[6] https://www.industry.gov.au/data-and-publications/estimating-greenhouse-gas-emissions-from-bushfires-in-australias-temperate-forests-focus-on-2019-20. Figure 5 in the document shows the areas significantly affected by the bushfires in July 2019 to January 2020. See also Phillips and Nogrady (2020).

Prediction of the 2019 springtime vortex weakening and its impact

To see how well the 2019 springtime SPV weakening and its impact on the SH surface climate were predicted, we first consider a multiple linear regression model to predict the SPVI. We use as predictors the PNJ at the stratopause (i.e., [U]' at 60°S, 1 hPa) in June-July and the partial poleward heat flux anomaly at 100 hPa in July-August, which is independent of the June-July PNJ by regressing out the covarying component with the PNJ from the heat flux anomaly[7] (Fig. 8). Based on the data over 1979-2018, the correlation of the predicted SPVI using the multiple linear regression model with the observed SPVI is 0.73 (using leave-one-year-out cross-validation[8]; Wilks 2006). This statistical model skilfully captures the magnitude of the 2019 event to be comparable to those of 2002 and 1988, the latter being another strong stratospheric warming event with a vortex displacement but without a wind reversal. A linear regression model with a single predictor, either the June-July PNJ or the July-August 100 hPa poleward heat flux, provides prediction skill of 0.63. However, the June-July PNJ alone underestimates the magnitudes of the 2019 and 1988 events (Fig. 8), while the July-August poleward heat flux alone underestimates the magnitude of the 2002 event. Therefore, this statistical model confirms that both the preconditioning provided by the poleward shift of the PNJ in early winter and subsequent anomalous wave activity flux from the troposphere into the stratosphere in late winter were important for the development of sustained weakening of the SH polar vortex in spring.

Predictability of SPV variability is further assessed using state-of-the-art dynamical seasonal forecast systems (Table 1). Our skill assessment is based on hindcasts over 1990-2012 (with a simple bias correction of using each model's anomalies relative to its

[7] June-July PNJ at 1 hPa and July-August poleward heat flux at 100 hPa is correlated by 0.48. While this covariation is naturally accounted for by multiple linear regression (Panofsky and Brier 1963), we have used the partial poleward heat flux at 100 hPa of July-August to assure the independence of the predictors.

[8] Similar skill is obtained with cross-validation processes leaving 5 or 10 years out.

392 climatology as a function of forecast lead time). Using the hindcasts, the SPVI is predictable,
393 as judged by temporal correlation skill (r) being 0.42, which is statistically significant at the
394 5% level (assessed by a two-tailed Student t-test with 23 independent forecast samples) from
395 as early as 1 July; and is skilfully predictable ($r > 0.6$) from early August (Fig. 9a; See also
396 Seviour et al. 2014, Byrne et al. 2019 and Hendon et al. 2020).

397 For the 2019 springtime SPV, the JMA, UKMO and ECMWF systems started
398 showing a sign of the weakening for forecasts initialized at the beginning of July (Fig. 9b).
399 Most of the systems predicted a substantially weaker vortex ($< -1\sigma$) for initializations in late
400 July and an extraordinary weakening ($< -2\sigma$) for initializations in late August, although there
401 was a drop in predictability in early to mid August. From the time when the vortex started its
402 sudden weakening and warming in the observations (i.e., late August to early September), the
403 BoM and UKMO systems, which are based on the same model, overpredicted the vortex
404 weakening and the ECMWF system underpredicted it relative to their standard deviations,
405 while NASA and JMA made skillful forecasts for it (Fig. 9b). In comparison, hindcast
406 predictions for the 2002 spring vortex weakening using the same systems show a similar lead
407 time dependence with an outstanding performance of the one-member NASA system
408 initialized in mid to late July, which then deteriorates in early-mid August before recovering
409 in late August (Fig. 9c).

410 An interesting aspect in Figure 9 is that predictions for the amplitude of the vortex
411 weakening varied by initialization dates only a few days apart for both 2002 and 2019, which
412 highlights the benefit of multiple forecast initialization times during a month and large
413 ensemble sizes to best capture the strength of the SH stratospheric polar vortex. The sharp
414 improvement in the model performance in predicting the strength of the 2019 springtime
415 vortex weakening for forecasts initialized closer to the event suggests that predictability of
416 the actual onset of the sudden warming and subsequent evolution of the polar vortex anomaly

417 throughout spring may be limited by the unpredictable components outside of the
418 deterministic range such as nonlinear wave amplification (e.g., Esler and Matthewman 2011;
419 Sjoberg and Birner 2014; Albers and Birner 2014) or tropospheric noise.

420 To see if the forecasts for the 2019 springtime SPV weakening correctly represent the
421 proposed low-frequency dynamical processes, we present the BoM forecasts initialized on 25
422 July 2019, which predicted the SPVI less than -1σ at the earliest (Fig. 9b). The 11-member
423 ensemble mean forecasts captured the increased upward propagating wave-1 activity and the
424 overall pattern of the lower tropospheric circulation anomalies in the SH high latitudes (Figs.
425 10a,b), demonstrating that a sequence of upward propagating wave events from the lower
426 troposphere acted to slow the upper stratospheric westerly jet. We further identified the three
427 ensemble members that predicted the least weakening of the springtime polar vortex (mean of
428 46 ms^{-1}) and the three ensemble members that predicted the most weakening (mean of 27 ms^{-1}).
429 We then formed the mean differences of [U] at 60°S, the wave-1 activity flux, and August
430 mean Z700 between the two groups. The differences show that stronger predicted vortex
431 weakening is associated with stronger anomalies of upward wave-1 activity flux (Fig. 10c),
432 consistent with the notion that the abrupt warming and deceleration of the vortex were driven
433 by the anomalous upward wave flux. Interestingly, the Z700 difference pattern for the three
434 weakest and strongest vortex forecasts (Fig. 10d) more highly resembles the observed
435 anomaly pattern than the ensemble mean anomaly pattern does (Fig. 10c), providing
436 reassurance that more vigorous wave-1 activity injected from the particular lower troposphere
437 anomaly pattern depicted in Fig. 10d is associated with a considerably weaker springtime
438 polar vortex. However, this analysis of ensemble spread implies that, although the model
439 confirms the proposed dynamics for the vortex weakening event taking a season, the precise
440 prediction of the magnitude and timing of the SSW was not predictable at this relatively long
441 lead time because of the stochastic nature of the upward wave activity flux.

We also examine the predictability of the SH surface climate anomalies in October to December 2019 that were promoted by the stratosphere-troposphere coupling in BoM forecasts. As the BoM system skilfully predicted the springtime SPV weakening with the initial conditions from late July, this system could make forecasts for the OND mean negative SAM with initial conditions of late July onwards (Fig. 11a). However, the prediction initialized on 9 August 2019 failed to produce the negative SAM because only a small reduction in the vortex strength was predicted (Fig. 9b), which implies the dependence of the predictability of late spring SAM on the predictability of the stratospheric polar vortex weakening. The 66 BoM forecasts from the six different initialization dates from late July till early September, represented by different color bars in Fig. 11a, further demonstrate a good linear fit between the forecasts of the springtime SPV weakening and OND negative SAM strengths (Fig. 11b).

We have shown in Figs. 6 and 7 that the SPV weakening and resultant negative SAM was a key driver of the extreme hot and dry conditions over subtropical eastern Australia, which contributed to one of Australia's worst wildfire seasons in the far eastern seaboard. To confirm that relationship in the prediction, we have plotted the forecast OND mean SAM versus the forecast OND mean Tmax and rainfall averaged over eastern Australia (east of 140°E) in Figs. 11c and 11d, respectively, using the 55 BoM forecasts initialized on 25 August and 1, 9, 17 and 25 September. The figures suggest that the more negative the SAM was, the hotter and drier eastern Australia was in the forecasts, as evidenced by the correlation of the forecast SAM with the forecast Tmax and rainfall being -0.41 and 0.44, respectively (statistically significant at the 0.2% level). These correlations represent independent evidence of the causal effect of the SAM on these impact-relevant quantities because the SAM is not strongly correlated with CP El Nino or the IOD in those forecasts. These relationships between the SAM and eastern Australian Tmax and rainfall forecasts of

OND are found in the ECMWF forecasts as well with even stronger correlations (Supplementary Fig. S10).

Concluding remarks

Seventeen years after the first-ever observed major SSW over Antarctica in late September 2002, an equivalently spectacular weakening and warming of the stratospheric polar vortex occurred in September 2019. The impact of the event on the SH surface climate lasted until the end of December. Thanks to advances in the capability of dynamical forecast systems and accumulated knowledge concerning the dynamics and impacts of SH stratospheric polar vortex variability since the 2002 SSW, the 2019 SSW received timely attention from researchers and forecasters, who were able to warn from late austral winter that there would be a high chance of its occurrence with potentially significant impacts on the SH surface climate throughout spring to the end of 2019 (Milinevsky et al. 2019; Hendon et al. 2019a,b). A review of the BoM service for 2019 reports "the BoM provided at least 104 briefings to governments, emergency services and likely affected sectors around the outlook for the fire season (spring and summer). It was recorded that in the 2019 fire season around 19 million hectares were burnt and 33 lives were lost. While horrific, these numbers may have been considerably higher without strategic decisions made through the close information sharing partnerships between the Bureau, Government and emergency services" (Climate Operations, BoM; internal communication, 2020).

In this study, we have provided a comprehensive overview of the monthly to seasonal timescale dynamics, climate impacts, and predictability of this remarkable event. Key findings are:

- The 2019 springtime stratospheric polar vortex weakening was as strong as that of 2002 despite not qualifying as a major SSW. New records were set in spring 2019 for

491 the vortex weakening at the stratopause, the Antarctic warming in the mid-
492 stratosphere and the high ozone concentration.

493 • The 2019 event closely followed the canonical development of SH springtime
494 stratospheric polar vortex weakening events with a poleward shifted polar night jet in
495 early winter and record-high monthly mean upward propagating wave-1 activity in
496 August, which emanated from the lower troposphere with distinctive anticyclonic
497 circulation anomalies centered over the Bellingshausen-Amundsen Seas.

498 • The 2019 stratospheric vortex weakening and warming coupled down to the surface
499 from mid-October, and the resultant record negative SAM induced significant local
500 climate extremes over eastern Australia, southern New Zealand, eastern South
501 America and western Patagonia through December 2019.

502 • Among the well-known large-scale drivers of Australian climate for its warm seasons,
503 the SH springtime polar vortex weakening appears to have been the most influential
504 contributor to the hot and dry and therefore fire-prone climate conditions over the
505 subtropical eastern seaboard of Australia, which suffered from severe and prolonged
506 wildfires during the late spring and early summer period.

507 • The occurrence of the 2019 springtime stratospheric vortex weakening was
508 foreseeable from July, and its extreme amplitude was skilfully predicted from late
509 August by the state-of-the-art forecast systems analyzed in this study.

510 • The skilful prediction of the 2019 springtime stratospheric vortex weakening resulted
511 in the skilful prediction of the late spring negative SAM, whose strength was tied to
512 the strength of hot and dry forecasts over eastern Australia for late spring.

513 We have covered some key aspects of the 2019 stratospheric polar vortex weakening,
514 but many interesting details of this event remain to be explored. For example, we reported
515 substantial amplitude of the wave-2 heat flux in July, but its source, interaction with wave-1,

and contribution to the vortex weakening are yet to be understood. Also, Hurwitz et al. (2011, 2014) and Lim et al. (2018) showed a possible relationship of the Antarctic stratospheric warming with central Pacific El Nino, which was present in 2019. Furthermore, the strong positive IOD and associated Rossby wave train was a dominant feature in the SH troposphere in late winter to early spring and might have interacted and/or interfered with the 2019 stratospheric vortex weakening and its downward coupling (e.g., Lim et al. 2020). Thus, atmospheric model experiments forced with the observed versus climatological boundary conditions may shed some light on the role of the extraordinary SST conditions of 2019 for the different stages of the 2019 stratospheric vortex evolution.

Finally, the near-record polar cap total column ozone concentration observed in spring 2019 appears to be largely driven by the stratospheric polar vortex weakening and record warming (e.g., Salby et al. 2002; Randel et al. 2002; Wargan et al. 2020), but ozone variations associated with the stratospheric polar vortex variations can feedback onto the circulation and temperature changes and amplify the impact of the vortex anomalies on the SAM in the troposphere (Hendon et al. 2020). Thus, how much of the negative SAM and associated SH surface climate extremes of October-December 2019 was driven by the ozone increase will be an interesting question to address, which will potentially benefit the future development effort of dynamical seasonal forecast systems, in which ozone is currently prescribed with monthly climatology (e.g., Seviour et al. 2014; Hendon et al. 2020) or radiatively not interactive (e.g., Johnson et al. 2018).

Acknowledgements

This study is part of the Forewarned is Forearmed project, which is supported by funding from the Australian Government Department of Agriculture as part of its Rural R&D for Profit programme. D. W. J. Thompson was supported by the NSF Climate and Large-Scale

Dynamics Program. A. Scaife and R. Comer were supported by the Met Office Hadley Centre Climate Programme funded by BEIS and Defra. P. A. Newman and L. Coy were supported by the NASA's Atmospheric Composition Modeling and Analysis Program. A. J. Dowdy was supported by the Victorian Government (DELWP) and Bushfire and Natural Hazards CRC project ERP14. H. Nakamura was supported by JSPS KAKENHI Grant P19H05702, Environment Research and Technology Development Fund (2–1904), ArCS-II Project (MEXT) and JST Belmont Forum CRA "InterDec". The authors are grateful to three anonymous reviewers for their thorough assessments and contructive feedback on the manuscript and Professor Andrew Dessler for his editorial effort for the peer-review process. Lim and Hendon thank their BoM colleagues - Matthew Wheeler and Hanh Nguyen for their constructive feedback on the initial version of the manuscript and Griffith Young and Morwenna Griffith for processing the BoM forecast data and the AWAP data; and thank Kelsey Druken at the National Computing Infrastructure (NCI) for her assistance with the BoM data archiving. This research was undertaken at the NCI National Facility in Canberra, Australia, which is supported by the Australian Commonwealth Government. The NCAR Command Language (NCL; http:// www.ncl.ucar.edu) version 6.4.0 was used for data analysis and visualization of the results. We also acknowledge NCAR/UCAR, NOAA/OAR/ESRL PSL, and the Japan Meteorological Agency for producing and providing the Hurrell et al. (2008) SST analysis, the Reynolds OI v2 SST analysis, GPCP v2.3 precipitation dataset, and the JRA-55 reanalysis, respectively.

References

Adler, R., and Coauthors, 2018: The Global Precipitation Climatology Project (GPCP) Monthly Analysis (New Version 2.3) and a Review of 2017 Global Precipitation. *Atmosphere (Basel).*, **9**, 138, doi:10.3390/atmos9040138. http://www.mdpi.com/2073-4433/9/4/138.

Albers, J. R., and T. Birner, 2014: Vortex preconditioning due to planetary and gravity waves prior to sudden stratospheric warmings. *J. Atmos. Sci.*, **71**, 4028–4054, doi:10.1175/JAS-D-14-0026.1.

Anstey, J. A., and T. G. Shepherd, 2014: High-latitude influence of the quasi-biennial oscillation. *Q. J. R. Meteorol. Soc.*, **140**, 1–21, doi:10.1002/qj.2132.

——, ——, and J. F. Scinocca, 2010: Influence of the quasi-biennial oscillation on the extratropical winter stratosphere in an atmospheric general circulation model and in reanalysis data. *J. Atmos. Sci.*, **67**, 1402–1419, doi:10.1175/2009JAS3292.1.

——, T. P. Banyard, N. Butchart, L. Coy, P. A. Newman, S. Osprey, and C. Wright, 2020: Quasi-biennial oscillation disrupted by abnormal Southern Hemisphere stratosphere. doi:doi.org/10.1002/essoar.10503358.1. https://www.essoar.org/doi/10.1002/essoar.10503358.1.

Ashok, K., S. K. Behera, S. A. Rao, H. Weng, and T. Yamagata, 2007: El Niño Modoki and its possible teleconnection. *J. Geophys. Res. Ocean.*, **112**, doi:10.1029/2006JC003798.

Baldwin, M. P., and T. J. Dunkerton, 2001: Stratospheric harbingers of anomalous weather regimes. *Science (80-.).*, **294**, 581–584, doi:10.1126/science.1063315.

——, and Coauthors, 2001: The quasi-biennial oscillation. *Rev. Geophys.*, **39**, 179–229, doi:10.1029/1999RG000073. http://doi.wiley.com/10.1029/1999RG000073.

583 Baldwin, M. P., T. Hirroka, A. O'Neill, and S. Yoden, 2003: Major stratospheric warming in
584 the SH in 2002. *SPARC Newsletter 20*
585 http://www.atmosp.physics.utoronto.ca/SPARC/News20/index.html.

586 Bett, P. E., K. E. Williams, C. Burton, A. A. Scaife, A. J. Wiltshire, and R. Gilham, 2020:
587 Skillful seasonal prediction of key carbon cycle components: NPP and fire risk. *Environ.*
588 *Res. Commun.*, **2**, 055002, doi:10.1088/2515-7620/ab8b29.

589 Birner, T., and J. R. Albers, 2017: Sudden Stratospheric Warmings and Anomalous Upward
590 Wave Activity Flux. *Sola*, **13A**, 8–12, doi:10.2151/sola.13A-002.
591 https://www.jstage.jst.go.jp/article/sola/13A/Special_Edition/13A_13A-002/_article.

592 Butler, A. H., D. J. Seidel, S. C. Hardiman, N. Butchart, T. Birner, and A. Match, 2015:
593 Defining sudden stratospheric warmings. *Bull. Am. Meteorol. Soc.*, **96**, 1913–1928,
594 doi:10.1175/BAMS-D-13-00173.1.

595 Byrne, N. J., and T. G. Shepherd, 2018: Seasonal persistence of circulation anomalies in the
596 Southern Hemisphere stratosphere and its implications for the troposphere. *J. Clim.*, **31**,
597 3467–3483, doi:10.1175/JCLI-D-17-0557.1.

598 ——, ——, and I. Polichtchouk, 2019: Subseasonal-to-Seasonal Predictability of the
599 Southern Hemisphere Eddy-Driven Jet During Austral Spring and Early Summer. *J.*
600 *Geophys. Res. Atmos.*, **124**, 6841–6855, doi:10.1029/2018JD030173.

601 Cai, W., P. van Rensch, T. Cowan, and H. H. Hendon, 2011: Teleconnection pathways of
602 ENSO and the IOD and the mechanisms for impacts on Australian rainfall. *J. Clim.*, **24**,
603 3910–3923, doi:10.1175/2011JCLI4129.1.

604 Ceppi, P., and D. L. Hartmann, 2013: On the speed of the eddy-driven jet and the width of the
605 Hadley cell in the Southern Hemisphere. *J. Clim.*, **26**, 3450–3465, doi:10.1175/JCLI-D-
606 12-00414.1.

607 Charlton, A. J., and L. M. Polvani, 2007: A New Look at Stratospheric Sudden Warmings .
608 Part I : Climatology and. 449–470.

609 Dowdy, A. J., 2018: Climatological variability of fire weather in Australia. *J. Appl. Meteorol.*
610 *Climatol.*, **57**, 221–234, doi:10.1175/JAMC-D-17-0167.1.

611 ——, R. A. Vincent, D. J. Murphy, M. Tsutsumi, D. M. Riggin, and M. J. Jarvis, 2004: The
612 large-scale dynamics of the mesosphere–lower thermosphere during the Southern
613 Hemisphere stratospheric warming of 2002. *Geophys. Res. Lett.*, **31**, L14102,
614 doi:10.1029/2004GL020282. http://doi.wiley.com/10.1029/2004GL020282.

615 Esler, J. G., and R. K. Scott, 2005: Excitation of Transient Rossby Waves on the
616 Stratospheric Polar Vortex and the Barotropic Sudden Warming. *J. Atmos. Sci.*, **62**,
617 3661–3682, doi:10.1175/JAS3557.1.
618 http://journals.ametsoc.org/doi/abs/10.1175/JAS3557.1.

619 ——, and N. J. Matthewman, 2011: Stratospheric sudden warmings as self-tuning
620 resonances. Part II: Vortex displacement events. *J. Atmos. Sci.*, **68**, 2505–2523,
621 doi:10.1175/JAS-D-11-08.1.

622 Esler, J. G., L. M. Polvani, and R. K. Scott, 2006: The Antarctic stratospheric sudden
623 warming of 2002: A self-tuned resonance? *Geophys. Res. Lett.*, **33**, 1–5,
624 doi:10.1029/2006GL026034.

625 Eswaraiah, S., J. Kim, W. Lee, J. Hwang, K. N. Kumar, and Y. H. Kim, 2020: Unusual
626 Changes in the Antarctic Middle Atmosphere During the 2019 Warming in the Southern
627 Hemisphere. *Geophys. Res. Lett.*, **47**, doi:10.1029/2020GL089199.
628 https://onlinelibrary.wiley.com/doi/10.1029/2020GL089199.

629 Garreaud, R., 2018: Record-breaking climate anomalies lead to severe drought and
630 environmental disruption in western Patagonia in 2016. *Clim. Res.*, **74**, 217–229,

631 doi:10.3354/cr01505. http://www.int-res.com/abstracts/cr/v74/n3/p217-229/.

632 Gong, D., and S. Wang, 1999: Definition of Antarctic Oscillation index. *Geophys. Res. Lett.*,
633 **26**, 459–462, doi:10.1029/1999GL900003.
634 http://doi.wiley.com/10.1029/1999GL900003.

635 Gray, L. J., M. J. Brown, J. Knight, M. Andrews, H. Lu, C. O'Reilly, and J. Anstey, 2020:
636 Forecasting extreme stratospheric polar vortex events. *Nat. Commun.*, **11**, 4630,
637 doi:10.1038/s41467-020-18299-7. http://www.nature.com/articles/s41467-020-18299-7.

638 Harnik, N., R. K. Scott, and J. Perlwitz, 2005: Wave reflectiom and focusing prior to the
639 major stratospheric warming of September 2002. *J. Atmos. Sci.*, **62**, 640–650,
640 doi:10.1175/JAS-3327.1.

641 Hendon, H. H., E.-P. Lim, and H. Nguyen, 2014: Seasonal variations of subtropical
642 precipitation associated with the Southern Annular Mode. *J. Clim.*, **27**, 3446–3460,
643 doi:10.1175/JCLI-D-13-00550.1.

644 ——, and Coauthors, 2019a: Rare forecasted climate event under way in the Southern
645 Hemisphere. *Nature*, **573**, 495–495, doi:10.1038/d41586-019-02858-0.
646 https://www.nature.com/articles/d41586-019-02858-0.

647 ——, A. B. Watkins, E.-P. Lim, and G. Young, 2019b: The air above Antarctica is suddenly
648 getting warmer – here's what it means for Australia. *The Conversation*
649 https://theconversation.com/the-air-above-antarctica-is-suddenly-getting-warmer-heres-
650 what-it-means-for-australia-123080.

651 ——, E.-P. Lim, and S. Abhik, 2020: Impact of Interannual Ozone Variations on the
652 Downward Coupling of the 2002 Southern Hemisphere Stratospheric Warming. *J.*
653 *Geophys. Res. Atmos.*, **125**, doi:10.1029/2020JD032952.
654 https://onlinelibrary.wiley.com/doi/10.1029/2020JD032952.

655 Hio, Y., and S. Yoden, 2005: Interannual variations of the seasonal march in the Southern
656 Hemisphere stratosphere for 1979–2002 and characterization of the unprecedented year
657 2002. *J. Atmos. Sci.*, **62**, 567–580, doi:10.1175/JAS-3333.1.
658 http://journals.ametsoc.org/doi/abs/10.1175/JAS-3333.1.

659 Holton, J. R., and H.-C. Tan, 1980: The Influence of the Equatorial Quasi-Biennial
660 Oscillation on the Global Circulation at 50 mb. *J. Atmos. Sci.*, **37**, 2200–2208,
661 doi:10.1175/1520-0469(1980)037<2200:TIOTEQ>2.0.CO;2.

662 Hudson, D., and Coauthors, 2017: ACCESS-S1: The new Bureau of Meteorology multi-week
663 to seasonal prediction system. *J. South. Hemisph. Earth Syst. Sci.*, **673**, 132–159,
664 doi:10.22499/3.6703.001.

665 Hurrell, J. W., J. J. Hack, D. Shea, J. M. Caron, and J. Rosinski, 2008: A new sea surface
666 temperature and sea ice boundary dataset for the community atmosphere model. *J.*
667 *Clim.*, **21**, 5145–5153, doi:10.1175/2008JCLI2292.1.

668 Hurwitz, M. M., P. A. Newman, L. D. Oman, and A. M. Molod, 2011: Response of the
669 Antarctic Stratosphere to Two Types of El Niño Events. *J. Atmos. Sci.*, **68**, 812–822,
670 doi:10.1175/2011JAS3606.1.
671 http://journals.ametsoc.org/doi/abs/10.1175/2011JAS3606.1.

672 Hurwitz, M. M., N. Calvo, C. I. Garfinkel, A. H. Butler, S. Ineson, C. Cagnazzo, E. Manzini,
673 and C. Peña-Ortiz, 2014: Extra-tropical atmospheric response to ENSO in the CMIP5
674 models. *Clim. Dyn.*, **43**, 3367–3376, doi:10.1007/s00382-014-2110-z.

675 Johnson, S. J., and Coauthors, 2018: SEAS5: The new ECMWF seasonal forecast system.
676 *Geosci. Model Dev. Discuss.*, 1–44, doi:10.5194/gmd-2018-228.

677 Jones, D. A., W. Wang, and R. Fawcett, 2009: High-quality spatial climate data-sets for
678 Australia. *Aust. Meteorol. Oceanogr. J.*, **58**, 233–248.

679 Jucker, M., 2016: Are sudden stratospheric warmings generic? Insights from an idealized
680 GCM. *J. Atmos. Sci.*, **73**, 5061–5080, doi:10.1175/JAS-D-15-0353.1.

681 Kang, S. M., L. M. Polvani, J. C. Fyfe, and M. Sigmond, 2011: Impact of polar ozone
682 depletion on subtropical precipitation. *Science (80-.).*, **332**, 951–954,
683 doi:10.1126/science.1202131.

684 Keeble, J., P. Braesicke, N. L. Abraham, H. K. Roscoe, and J. A. Pyle, 2014: The impact of
685 polar stratospheric ozone loss on southern Hemisphere stratospheric circulation and
686 climate. *Atmos. Chem. Phys.*, **14**, 13705–13717, doi:10.5194/acp-14-13705-2014.

687 Kidston, J., A. A. Scaife, S. C. Hardiman, D. M. Mitchell, N. Butchart, M. P. Baldwin, and L.
688 J. Gray, 2015: Stratospheric influence on tropospheric jet streams, storm tracks and
689 surface weather. *Nat. Geosci.*, **8**, 433–440, doi:10.1038/ngeo2424.
690 http://www.nature.com/doifinder/10.1038/ngeo2424.

691 Kodera, K., and Y. Kuroda, 2002: Dynamical response to the solar cycle. *J. Geophys. Res.*
692 *Atmos.*, **107**, 1–12, doi:10.1029/2002JD002224.

693 Kuroda, Y., and K. Kodera, 1998: Interannual variability in the troposphere and stratosphere
694 of the Southern Hemisphere winter. *J. Geophys. Res. Atmos.*, **103**, 13787–13799,
695 doi:10.1029/98JD01042. http://doi.wiley.com/10.1029/98JD01042.

696 Lawrence, Z. D., and G. L. Manney, 2020: Does the Arctic Stratospheric Polar Vortex
697 Exhibit Signs of Preconditioning Prior to Sudden Stratospheric Warmings ? *J. Atmos.*,
698 611–632, doi:10.1175/JAS-D-19-0168.1.

699 Lim, E.-P., H. H. Hendon, and D. W. J. Thompson, 2018: Seasonal evolution of stratosphere-
700 troposphere coupling in the Southern Hemisphere and implications for the predictability
701 of surface climate. *J. Geophys. Res. Atmos.*, **123**, 12,002–12,016,
702 doi:10.1029/2018JD029321. http://doi.wiley.com/10.1029/2018JD029321.

703 Lim, E.-P., H. H. Hendon, G. Boschat, D. Hudson, D. W. J. Thompson, A. J. Dowdy, and J.
704 M. Arblaster, 2019: Australian hot and dry extremes induced by weakenings of the
705 stratospheric polar vortex. *Nat. Geosci.*, **12**, 896–901, doi:10.1038/s41561-019-0456-x.
706 http://dx.doi.org/10.1038/s41561-019-0456-x.

707 ——, and Coauthors, 2020: The 2019 Antarctic sudden stratospheric warming. *SPARC*
708 *Newsletter 54*.

709 MacLachlan, C., and Coauthors, 2015: Global Seasonal forecast system version 5 (GloSea5):
710 A high-resolution seasonal forecast system. *Q. J. R. Meteorol. Soc.*, **141**, 1072–1084,
711 doi:10.1002/qj.2396.

712 Marshall, G. J., 2003: Trends in the Southern Annular Mode from observations and
713 reanalyses. *J. Clim.*, **16**, 4134–4143, doi:10.1175/1520-
714 0442(2003)016<4134:TITSAM>2.0.CO;2.

715 Matsuno, T., 1970: Vertical Propagation of Stationary Planetary Waves in the Winter
716 Northern Hemisphere. *J. Atmos. Sci.*, **27**, 871–883, doi:10.1175/1520-
717 0469(1970)027<0871:VPOSPW>2.0.CO;2.
718 http://journals.ametsoc.org/doi/abs/10.1175/1520-
719 0469%281970%29027%3C0871%3AVPOSPW%3E2.0.CO%3B2.

720 McIntyre, M. E., 1982: How well do we understand the dynamics of stratospheric warmings?
721 *J. Meteorol. Soc. Japan*, 37–65.

722 McIntyre, M. E., and T. N. Palmer, 1983: Breaking planetary waves in the stratosphere.
723 *Nature*, **305**, 593–600, doi:10.1038/305593a0.
724 http://www.nature.com/articles/305593a0.

725 Milinevsky, G., O. Evtushevsky, A. Klekociuk, Y. Wang, A. Grytsai, V. Shulga, and O.
726 Ivaniha, 2019: Early indications of anomalous behavior in the 2019 spring ozone hole

over Antarctica. http://arxiv.org/abs/1909.07574.

Molod, A., and Coauthors, 2020: GEOS-S2S Version 2: The GMAO High-Resolution Coupled Model and Assimilation System for Seasonal Prediction. *J. Geophys. Res. Atmos.*, **125**, doi:10.1029/2019JD031767. https://agupubs.onlinelibrary.wiley.com/doi/abs/10.1029/2019JD031767.

Newman, P., and E. Nash, 2005: The unusual Southern Hemisphere stratosphere winter of 2002. *J. Atmos. Sci.*, **62**, 614–628, doi:10.1175/JAS-3323.1. http://journals.ametsoc.org/doi/abs/10.1175/JAS-3323.1.

Newman, P. A., E. R. Nash, and J. E. Rosenfield, 2001: What controls the temperature of the Arctic stratosphere during the spring? *J. Geophys. Res. Atmos.*, **106**, 19999–20010, doi:10.1029/2000JD000061. https://agupubs.onlinelibrary.wiley.com/doi/epdf/10.1029/2000JD000061.

Nishii, K., and H. Nakamura, 2004: Tropospheric influence on the diminished Antarctic ozone hole in September 2002. *Geophys. Res. Lett.*, **31**, doi:10.1029/2004GL019532.

Noguchi, S., Y. Kuroda, K. Kodera, and S. Watanabe, 2020: Robust Enhancement of Tropical Convective Activity by the 2019 Antarctic Sudden Stratospheric Warming. *Geophys. Res. Lett.*, **47**, doi:10.1029/2020GL088743. https://onlinelibrary.wiley.com/doi/10.1029/2020GL088743.

Panofsky, H. A., and G. W. Brier, 1963: *Some Applications of Statistics to Meteorology*. 1st editio. Pennsylvania State University,.

Peixoto, J. P., and A. H. Oort, 1992: *Physics of Climate*. 1st ed. AIP-Press, XXXIX, 520 pp.

Phillips, N., and B. Nogrady, 2020: The race to decipher how climate change influenced Australia's record fires. *Nature*, **577**, 610–612. https://www.nature.com/articles/d41586-020-00173-7.

751 Randel, W. J., F. Wu, and R. S. Stolarski, 2002: Changes in Column Ozone Correlated with
752 the Stratospheric EP Flux. *J. Meteorol. Soc. Japan*, **80**, 849–862,
753 doi:10.2151/jmsj.80.849.
754 http://joi.jlc.jst.go.jp/JST.JSTAGE/jmsj/80.849?from=CrossRef.

755 Rao, J., C. I. Garfinkel, I. P. White, and C. Schwartz, 2020: The Southern Hemisphere Minor
756 Sudden Stratospheric Warming in September 2019 and its Predictions in S2S Models. *J.*
757 *Geophys. Res. Atmos.*, **125**, 1–19, doi:10.1029/2020JD032723.

758 Reisinger, A., R. L. Kitching, F. Chiew, L. Hughes, P. C. D. Newton, S. S. Schuster, A. Tait,
759 and P. H. Whetton, 2014: Australasia. *Climate Change 2014: Impacts, Adaptation, and*
760 *Vulnerability. Part B: Regional Aspects. Contribution of Working Group II to the Fifth*
761 *Assessment Report of the Intergovernmental Panel on Climate Change [Barros, V.R.,*
762 *C.B. Field, D.J. Dokken, M.D. Mastrandre*, 1371–1438.

763 Reynolds, R. W., N. A. Rayner, T. M. Smith, D. C. Stokes, and W. Wang, 2002: An
764 improved in situ and satellite SST analysis for climate. *J. Clim.*, **15**, 1609–1625,
765 doi:10.1175/1520-0442(2002)015<1609:AIISAS>2.0.CO;2.

766 Saji, N. H., and T. Yamagata, 2003: Possible impacts of Indian Ocean Dipole mode events on
767 global climate. *Clim. Res.*, **25**, 151–169, doi:10.3354/cr025151.

768 ——, B. N. Goswami, P. N. Vinayachandran, and T. Yamagata, 1999: A dipole mode in the
769 tropical Indian Ocean. *Nature*, **401**, 360–363, doi:10.1038/43854.
770 http://www.nature.com/nature/journal/v401/n6751/full/401360a0.html%5Cnhttp://www.
771 nature.com/nature/journal/v401/n6751/pdf/401360a0.pdf.

772 Salby, M., P. Callaghan, and M. Guirlet, 2002: Interannual changes of temperature and
773 ozone : Relationship between the lower and upper stratosphere. *J. Geophys. Res.*, **107**,
774 1–8, doi:10.1029/2001JD000421.

775 Scaife, A. A., D. R. Jackson, R. Swinbank, N. Butchart, H. E. Thornton, M. Keil, and L.
776 Henderson, 2005: Stratospheric Vacillations and the Major Warming over Antarctica in
777 2002. *J. Atmos. Sci.*, **62**, 629–639, doi:10.1175/JAS-3334.1.

778 Scott, R. K., and L. M. Polvani, 2004: Stratospheric control of upward wave flux near the
779 tropopause. *Geophys. Res. Lett.*, **31**, 1–4, doi:10.1029/2003GL017965.

780 Seviour, W. J. M., S. C. Hardiman, L. J. Gray, N. Butchart, C. MacLachlan, and A. A. Scaife,
781 2014: Skillful seasonal prediction of the Southern Annular Mode and Antarctic ozone. *J.*
782 *Clim.*, **27**, 7462–7474, doi:10.1175/JCLI-D-14-00264.1.
783 http://journals.ametsoc.org/doi/abs/10.1175/JCLI-D-14-00264.1.

784 Shen, X., L. Wang, and S. Osprey, 2020: Tropospheric forcing of the 2019 Antarctic sudden
785 stratospheric warming. *Geophys. Res. Lett.*, doi:10.1029/2020GL089343.

786 Shepherd, T., R. A. Plumb, and S. C. Wofsy, 2005: PREFACE. *J. Atmos. Sci.*, **62**, 565–566,
787 doi:10.1175/JAS3562.1.

788 Shepherd, T. G., 2019: Storyline approach to the construction of regional climate change
789 information. *Proc. R. Soc. A Math. Phys. Eng. Sci.*, **475**, doi:10.1098/rspa.2019.0013.

790 Shiotani, M., N. Shimoda, and I. Hirota, 1993: Interannual variability of the stratospheric
791 circulation in the Southern Hemisphere. *Q. J. R. Meteorol. Soc.*, **119**, 531–546.

792 Sjoberg, J. P., and T. Birner, 2014: Stratospheric wave-mean flow feedbacks and sudden
793 stratospheric warmings in a simple model forced by upward wave activity flux. *J.*
794 *Atmos. Sci.*, **71**, 4055–4071, doi:10.1175/JAS-D-14-0113.1.

795 Stolarski, R. S., R. D. McPeters, and P. a. Newman, 2005: The Ozone Hole of 2002 as
796 Measured by TOMS. *J. Atmos. Sci.*, **62**, 716–720, doi:10.1175/JAS-3338.1.

797 Taguchi, M., and S. Yoden, 2002: Internal Interannual Variability of the Troposphere–

798 Stratosphere Coupled System in a Simple Global Circulation Model. Part I: Parameter
799 Sweep Experiment. *J. Atmos. Sci.*, **59**, 3021–3036, doi:10.1175/1520-
800 0469(2002)059<3021:IIVOTT>2.0.CO;2.

801 Takaya, Y., and Coauthors, 2018: Japan Meteorological Agency/Meteorological Research
802 Institute-Coupled Prediction System version 2 (JMA/MRI-CPS2): atmosphere–land–
803 ocean–sea ice coupled prediction system for operational seasonal forecasting. *Clim.*
804 *Dyn.*, **50**, 751–765, doi:10.1007/s00382-017-3638-5.
805 http://link.springer.com/10.1007/s00382-017-3638-5.

806 Thompson, D. W. J., and J. M. Wallace, 2000: Annular Mode in the extratropical circulation.
807 Part I : Month-to-month variability. *J. Clim.*, **13**, 1000–1016,
808 doi:http://dx.doi.org/10.1175/1520-0442(2000)013<1000:AMITEC>2.0.CO;2.
809 papers2://publication/uuid/9A9E1710-F09C-4477-B3E2-BB99F78E6CA4.

810 Thompson, D. W. J., M. P. Baldwin, and S. Solomon, 2005: Stratosphere–troposphere
811 coupling in the Southern Hemisphere. *J. Atmos. Sci.*, **62**, 708–715, doi:10.1175/JAS-
812 3321.1. http://journals.ametsoc.org/doi/abs/10.1175/JAS-3321.1.

813 Wang, G., and H. H. Hendon, 2007: Sensitivity of Australian Rainfall to Inter–El Niño
814 Variations. *J. Clim.*, **20**, 4211–4226, doi:10.1175/JCLI4228.1.

815 Wargan, K., B. Weir, G. L. Manney, S. E. Cohn, and N. J. Livesey, 2020: The anomalous
816 2019 Antarctic ozone hole in the GEOS Constituent Data Assimilation System with
817 MLS observations. *J. Geophys. Res. Atmos.*, 1–28, doi:10.1029/2020jd033335.

818 Wilks, D. S., 2006: *Statistical methods in the atmospheric sciences*. Second Edi. Academic
819 Press, Inc., 592 pp.

820 Yamazaki, Y., and Coauthors, 2020: September 2019 Antarctic sudden stratospheric
821 warming: quasi-6-day wave burst and ionospheric effects. *Geophys. Res. Lett.*,

822 2019GL086577, doi:10.1029/2019GL086577.

823 https://onlinelibrary.wiley.com/doi/abs/10.1029/2019GL086577.

824

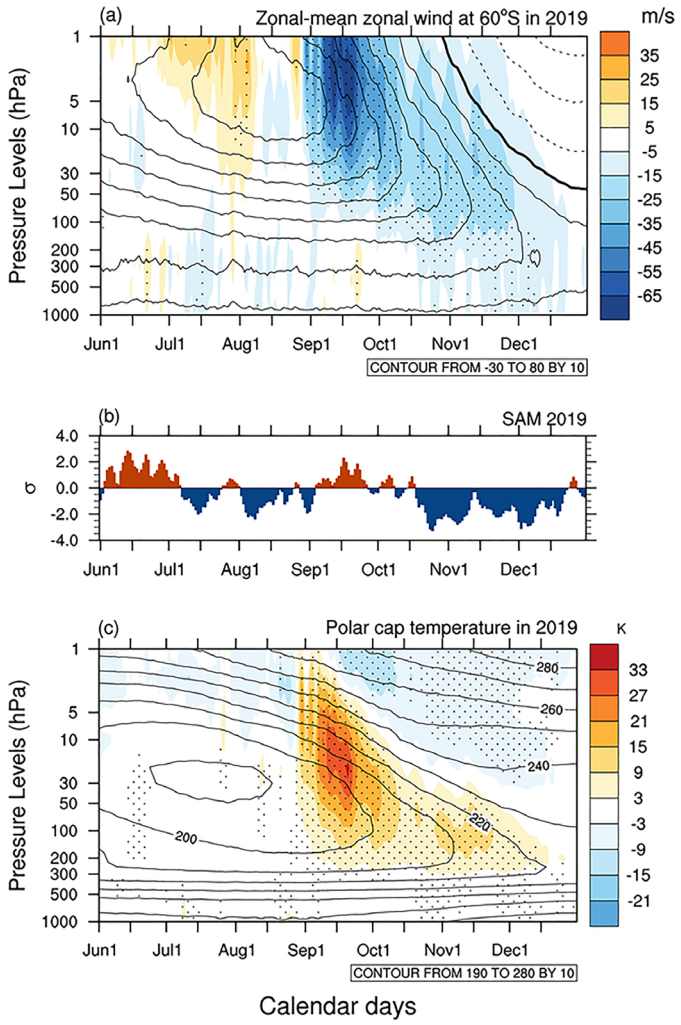

825

826 **FIG. 1**. Daily anomalies of (a) zonal-mean zonal wind ([U]') at 60°S from 1000 to 1 hPa; (b)
827 SAM as monitored by the Antarctic Oscillation (AAO) index by NOAA Climate Prediction
828 Center (CPC); and (c) Antarctic polar cap temperatures averaged over 60-90°S. Time runs
829 from June 1 to December 31 in 2019. The daily CPC AAO index in (b) is obtained by
830 projecting daily 700-hPa geopotential height (Z700) anomalies onto the leading mode of the
831 empirical orthogonal function (EOF) of monthly mean Z700 variability over the domain 20-
832 90°S (Thompson and Wallace 2000). In (a) and (c) color shading indicates anomalies, and the
833 overlayed contours indicate the climatologies computed over 1979-2018. Color shading
834 intervals are (a) 10 ms^{-1} and (c) 6 K, and contour intervals are (a) 10 ms^{-1} and (c) 10 K,
835 respectively. Stippling in (a) and (c) denote the 2019 anomalies fall in the ±5% tails of the
836 climatological distribution as judged by the anomalies being greater than 1.68 standard
837 deviations (σ) or less than -1.68 σ, where σ is computed over 1979-2018.

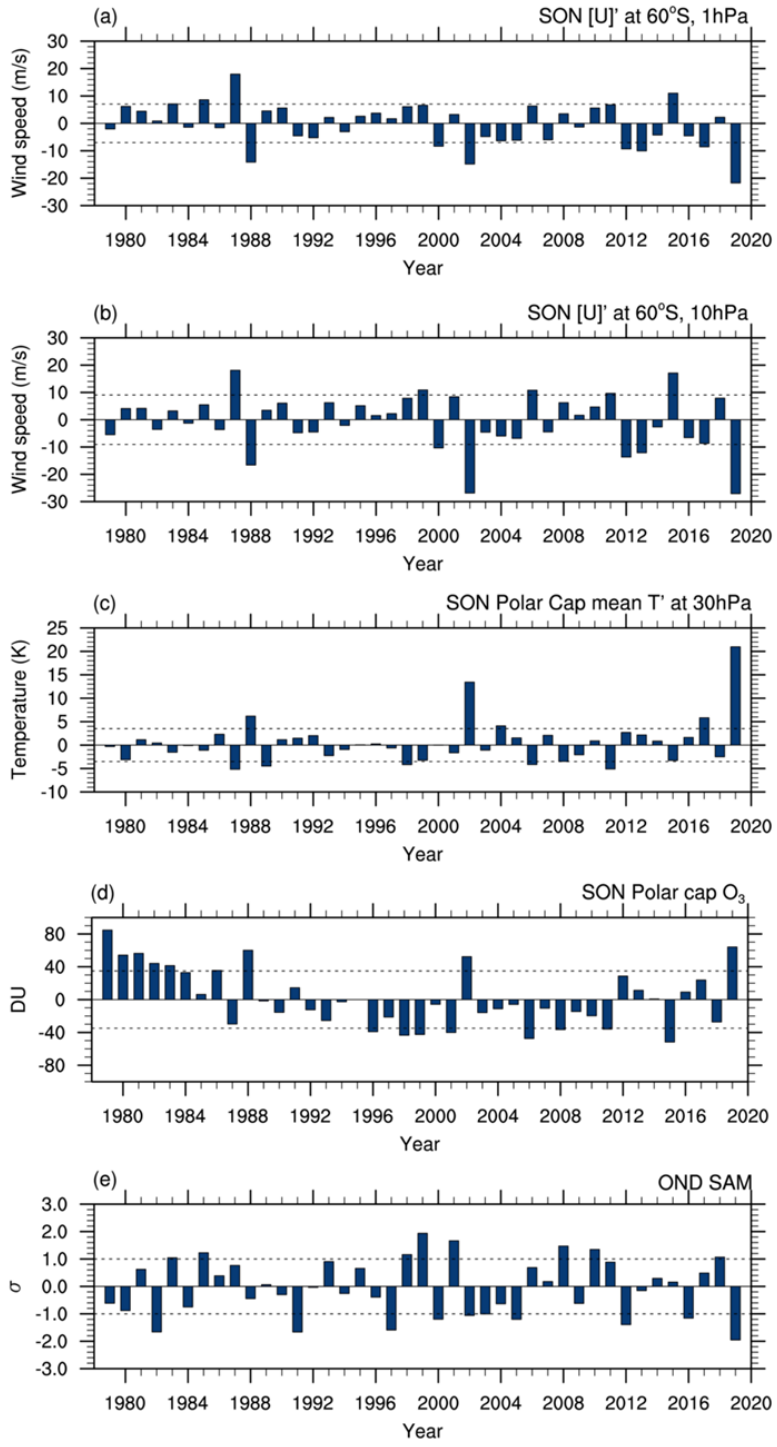

838

839 **FIG. 2.** Time series of anomalies of (a) September-November mean (SON) [U]' at 60°S at 1
840 hPa; (b) same as (a) but at 10 hPa (i.e., the stratospheric polar vortex index, SPVI); (c) SON
841 Antarctic temperature south of 60°S at 30 hPa; (d) SON Antarctic polar cap ozone (the data
842 of total column ozone averaged over the polar cap south of 63°S were obtained from the
843 NASA Ozone Watch page (https://ozonewatch.gsfc.nasa.gov/)); and (e) standardized
844 October-December mean (OND) SAM (NOAA CPC monthly AAO) index. The dashed
845 horizontal lines in each panel indicates a unit standard deviation.

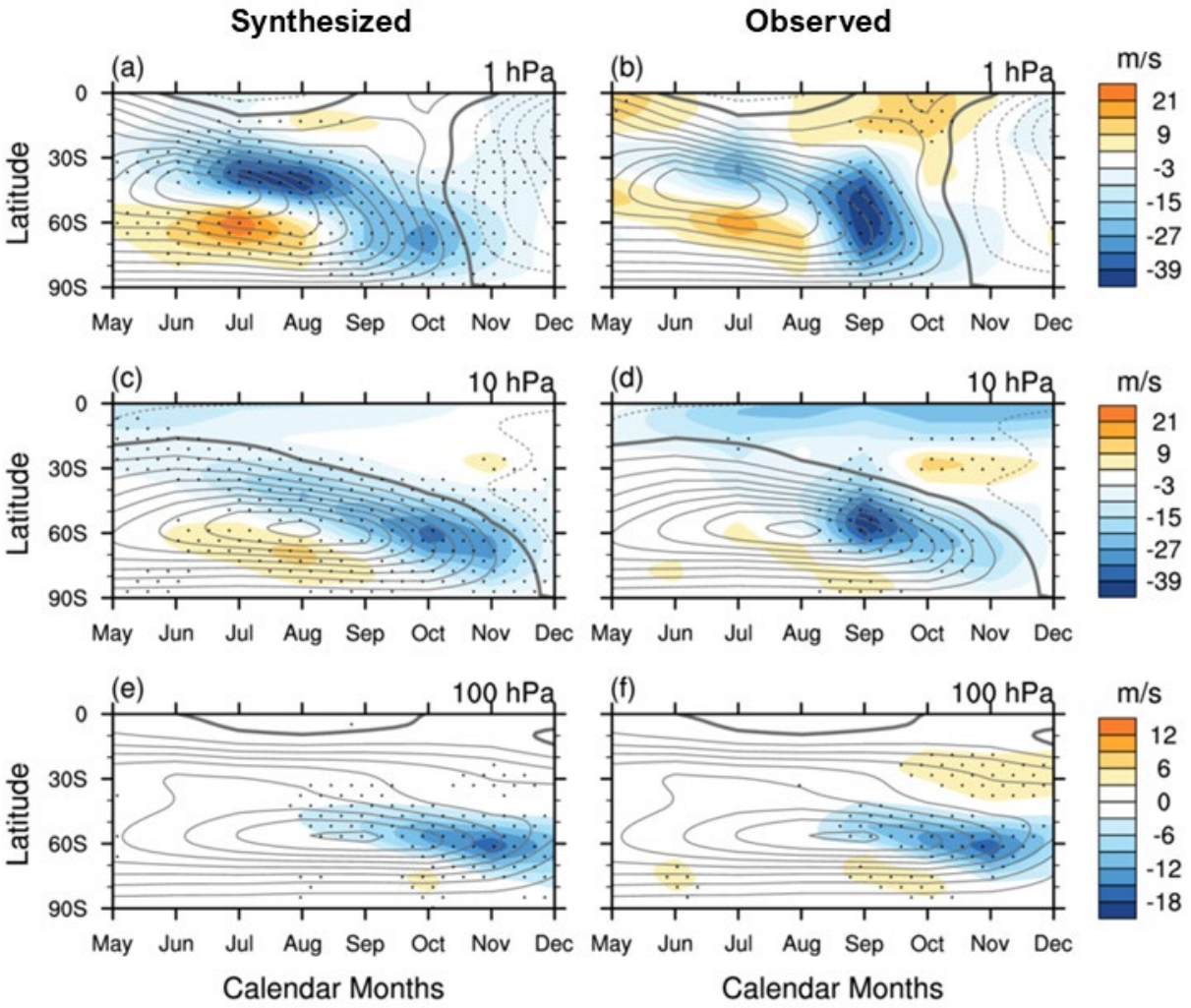

FIG 3. Latitude-time sections of monthly mean anomalies of zonal-mean zonal wind ([U]') at (top) 1 hPa, (middle) 10 hPa and (bottom) 100 hPa. (Left panels) (a), (c) and (e) Syntheses of 2019 by regressing [U]' at 1, 10 and 100 hPa onto the SPVI shown in FIG 2b for 1979-2018 and scaling the regression coefficients by the 2019 index magnitude (see Supplemental Material for further details). (Right panels) (b), (d) and (f) 2019 observed [U]' at 1, 10 and 100 hPa, respectively. Color shading indicates anomalies, and contours indicate the climatological winds. Color shading intervals are 6 ms^{-1} in (a-d) and 3 ms^{-1} in (e,f), and contour intervals are 10 ms^{-1} in (a-d) and 5 ms^{-1} in (e,f). Zero contours are thickened and negative contours are dashed. Stippling in the left panels denotes statistical significance of the regression coefficients at the 10% level, assessed by a two-tailed Student t-test with 40 samples, and stippling in the right panels denotes extreme anomalies in the ±5% tails of the climatological distribution as described in FIG 1.

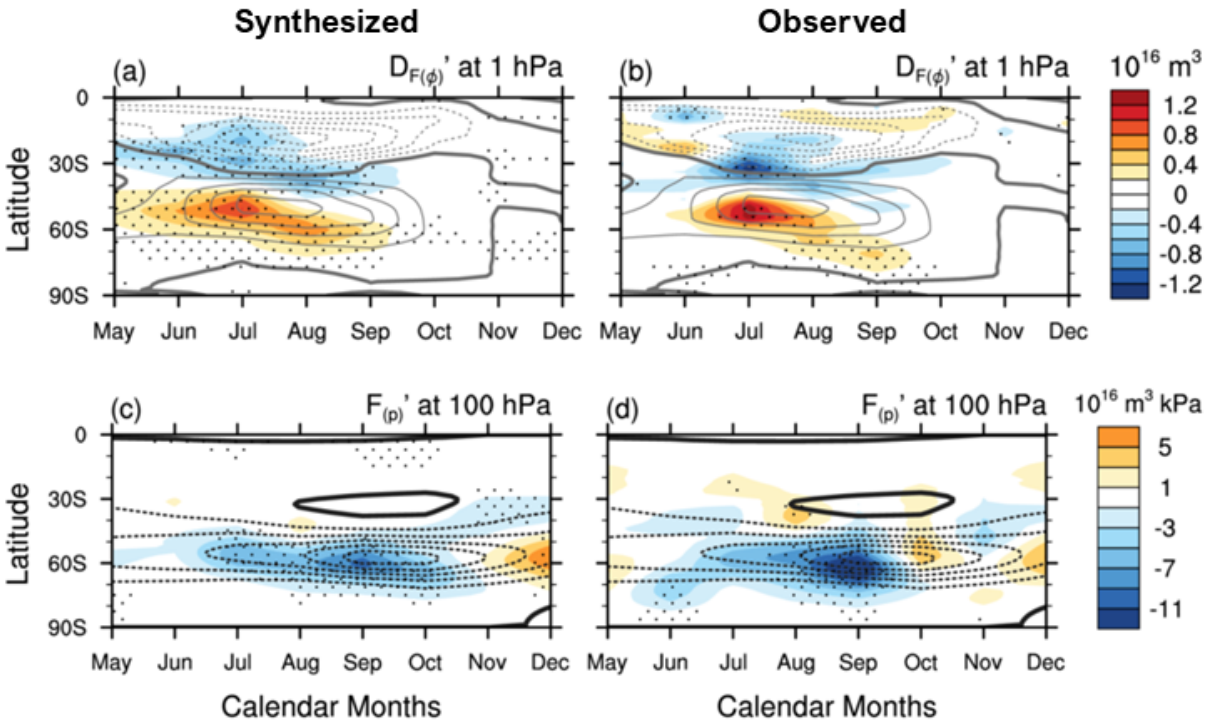

859

860 **FIG 4.** As in FIG 3 except for (top) the monthly mean anomalies of Eliassen-Palm (E-P) flux
861 divergence ($D_{F(\varphi)}$') by the horizontal component ($F_{(\varphi)}$) (i.e., momentum flux convergence) at
862 1 hPa and (bottom) the vertical component of the E-P flux ($F_{(p)}$'; i.e., poleward eddy heat
863 flux) at 100 hPa. In (c) and (d) negative values indicate the southward (i.e., poleward) heat
864 flux in the SH representing upward wave propagation. The E-P flux and its divergence were
865 computed on the spherical coordinate following Peixoto and Oort (1992). Color shading and
866 contours show anomalies and climatologies, respectively, of $D_{F(\varphi)}$ and $F_{(p)}$. The color shading
867 interval is $0.2*10^{16}$ m^3 for $D_{F(\varphi)}$' and $2.0*10^{16}$ m^3*kPa for $F_{(p)}$', and the contour interval is
868 $0.2*10^{16}$ m^3 for $D_{F(\varphi)}$ and $2.0*10^{16}$ m^3*kPa for $F_{(p)}$. Stippling indicates the statistical
869 significance as described in FIG3.

870

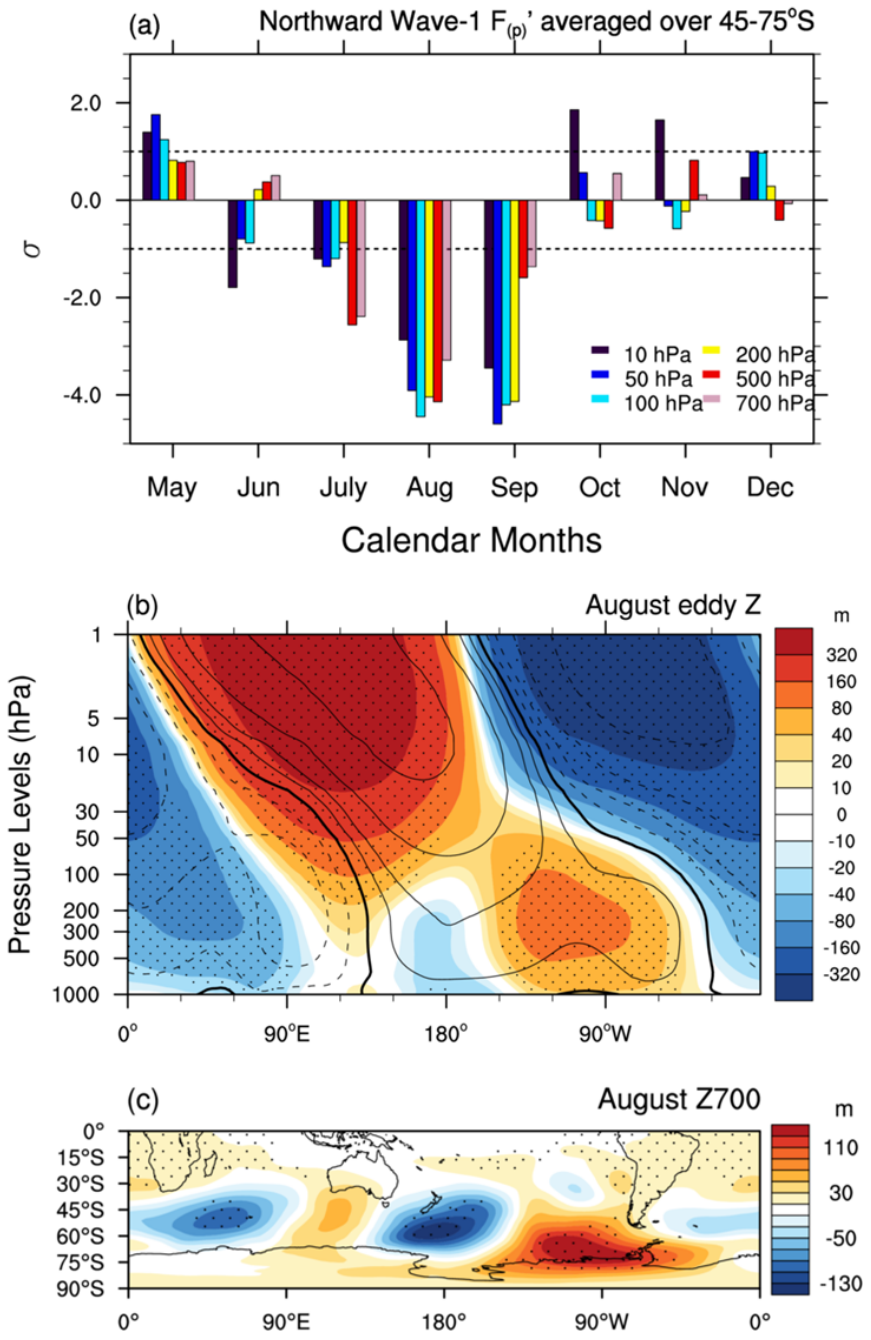

871

872 **FIG 5.** (a) Standardized anomalies of poleward wave-1 heat flux ($F_{(p)}$') averaged over 45-
873 75°S (with cosine weighting) at different vertical levels. (b) August eddy geopotential height
874 (Z) averaged over 45-75°S with cosine latitude weighting. The contours and color shadings
875 indicate climatological and 2019 eddy patterns, respectively. (c) Z700 anomalies for August
876 2019. In (b) the color shading interval starts from -10 and 10 m and increases by two-folds,
877 and the contour interval does the same but starting from -20 and 20 m. In (c) the color
878 shading inverval is 20 m. Stippling in (b) and (c) indicates extremity of anomalies found at
879 the ±5% tails of the climatological distribution as described in FIG 3.

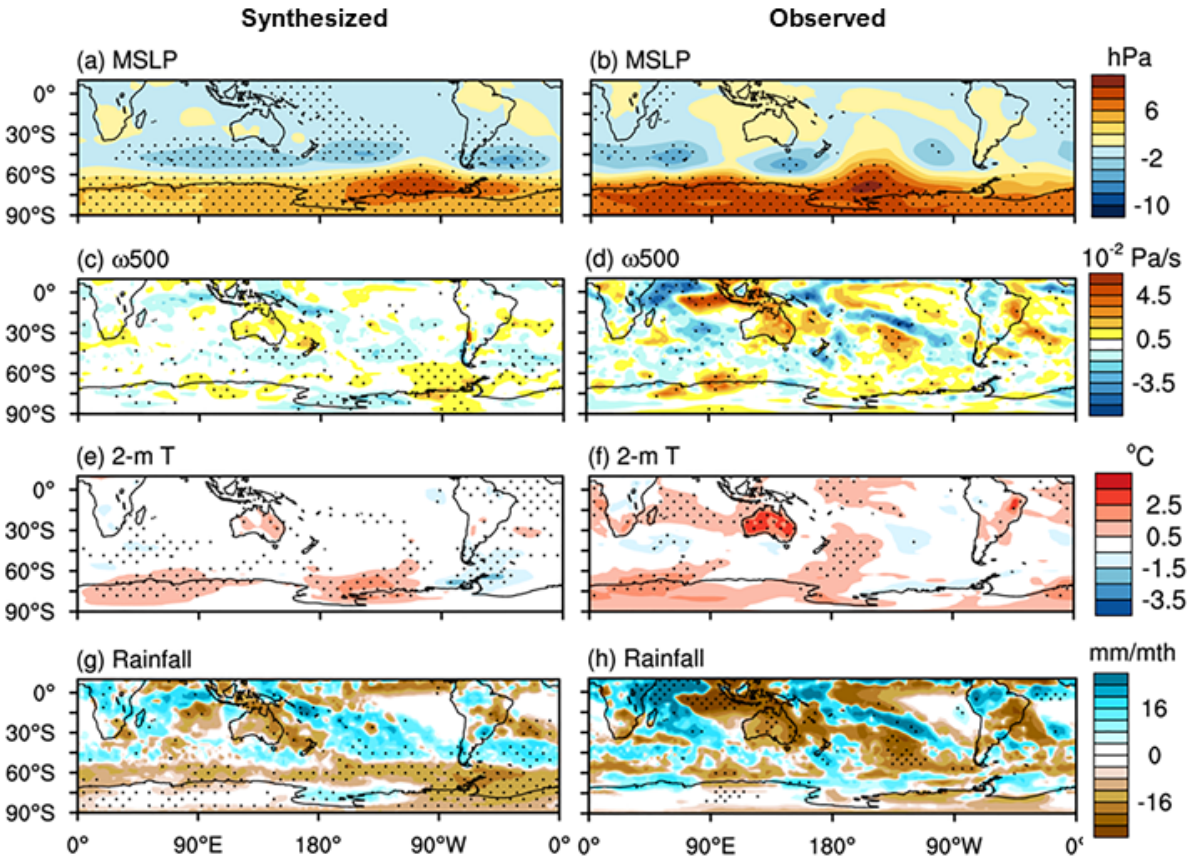

FIG 6. (Left panels) Syntheses of 2019 OND mean (a) mean sea level pressure (MSLP), (c) vertical velocity (ω) at 500 hPa, (e) 2-m air temperature and (g) rainfall anomalies derived from the regression onto the SPVI as described in FIG 3. The color shading interval is 2 hPa in (a), 0.01 Pa s^{-1} in (c), and 1 °C in (e). The color shading interval in (g) increases by two-folds for each level from 2 mm $month^{-1}$. (Right panels) Same as the left panels but the observed anomalies of 2019. Stippling indicates the statistical significance as described in FIG 3 except in (h) where stippling shows where the rainfall anomalies are found in the top and bottom decile categories.

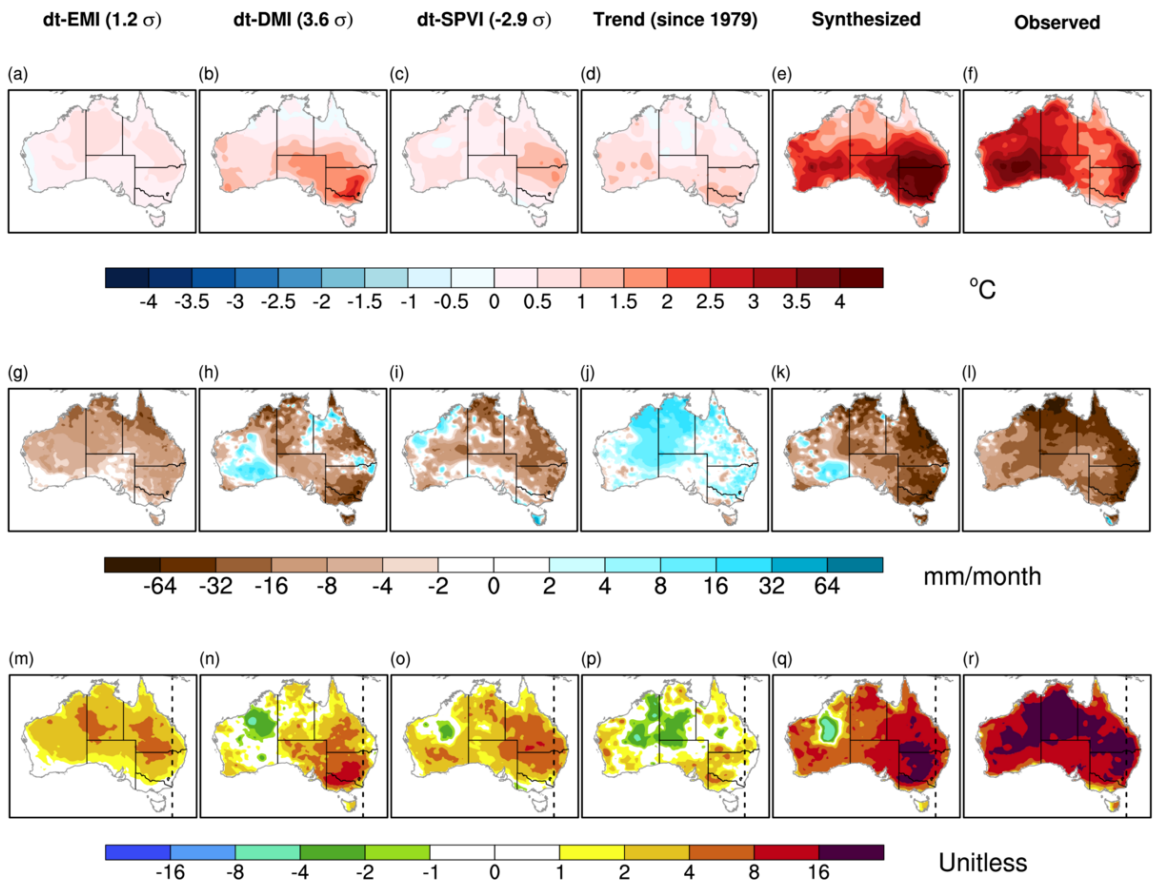

FIG 7. Patterns of OND mean Australian (top row; a-d) daily maximum temperatures; (middle row; g-j) rainfall; and (bottom row; m-p) daily forest fire danger index (FFDI) anomalies explained by (a,g,m) the de-trended El Nino Modoki Index (dt-EMI); (b,h,n) the de-trended Indian Ocean Dipole mode index (dt-DMI); (c,i,o) the de-trended spring polar vortex index (dt-SPVI; Fig. 2a); and (d,j,p) a linear trend of OND, using multiple linear regression built for 1979-2018. The regression coefficients are scaled by the 2019 amplitudes of the predictors as indicated by the numbers in the parentheses in the column titles. The synthesized anomalies of 2019 by the multiple linear regression model are displayed in (e), (k) and (q), and the observed anomalies of 2019 are displayed in (f),(l) and (r). The contour interval in the top panels is 0.5°C, while the intervals in the middle and bottom panels for respective rainfall and FFDI increase by two-fold for each level. The dashed vertical line in (m-r) marks 150°E as the area east of it experienced intense and prolonged bushfires in the OND season in 2019.

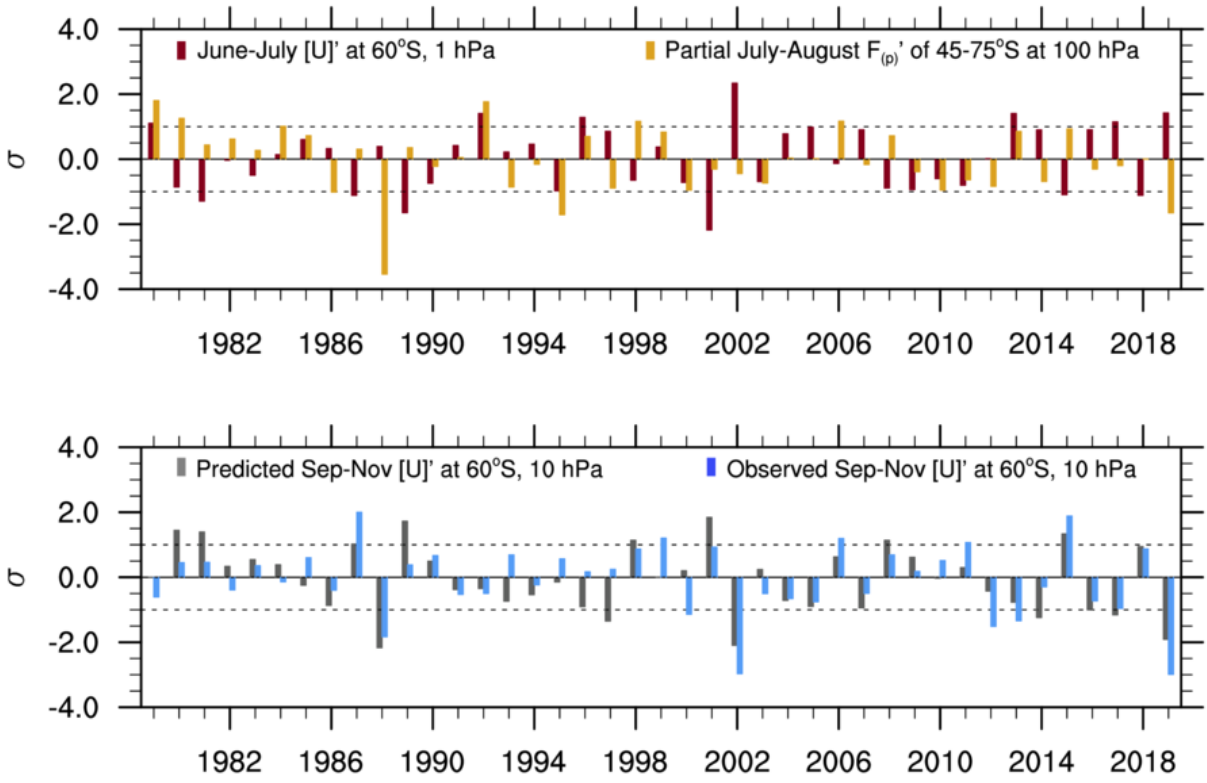

906

907

908 **FIG 8.** (Upper panel) Time series of June-July mean PNJ ([U]' at 60°S) at 1 hPa (red bars),
909 partial July-August mean northward heat flux ($F_{(p)}$') independent of the June-July PNJ at 1
910 hPa (orange bars); and (lower panel) statistically predicted SPVI (gray bars). The observed
911 SPVI shown in FIG 2b is displayed in the lower panel again with light blue bars for
912 comparison. The time series are normalized by their respective standard deviation (σ)
913 obtained in 1979-2018. The horizontal dashed lines indicate |1 σ|.

914

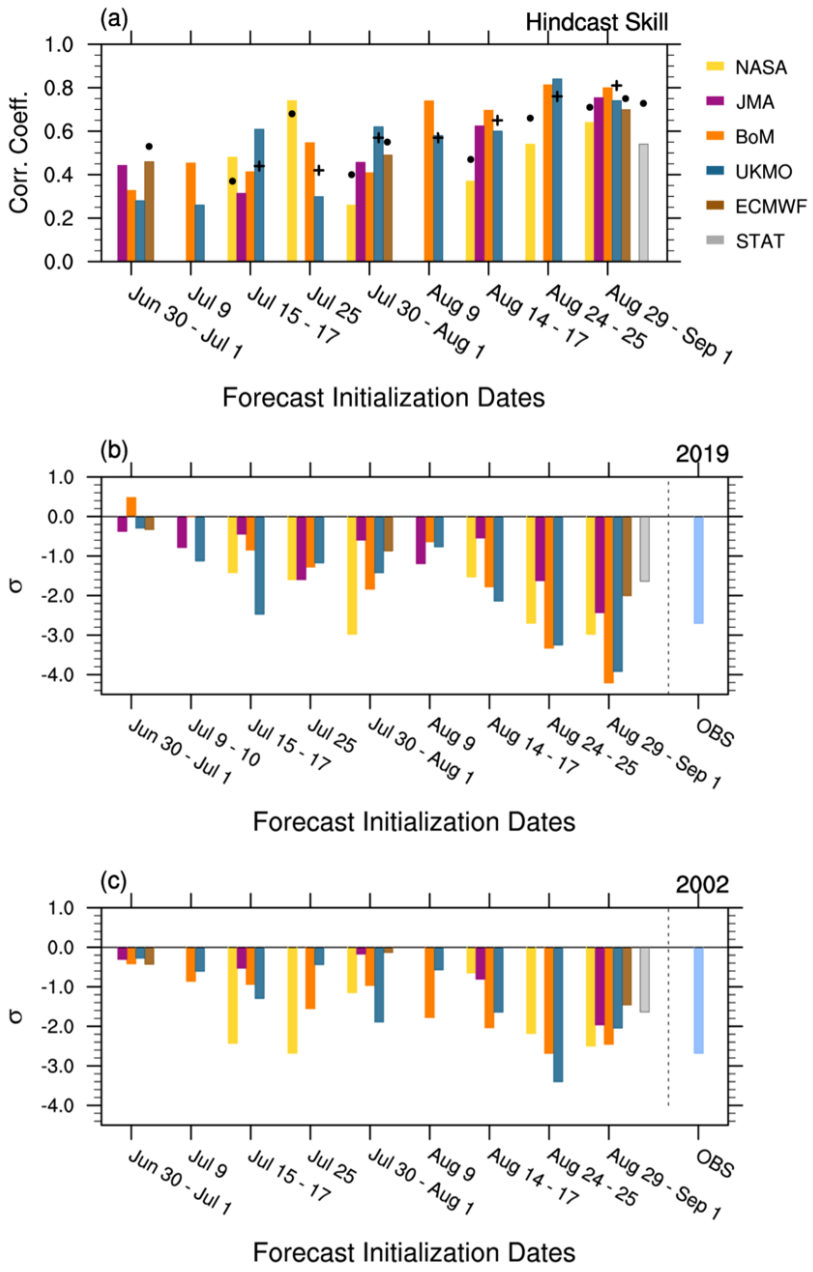

915

916 **FIG 9.** (a) Hindcast skill to predict the SPVI (as defined with FIG. 2b; SON [U]' at 60°S at
917 10 hPa) from the five different operational center S2S forecast systems – NASA GEOS-S2S-
918 2 (yellow), JMA/MRI-CPS2 (purple), BoM) ACCESS-S1 (orange), UKMO GloSea-5 (blue),
919 and ECMWF-SEAS5 (brown). Skill of the statistical prediction discussed with Figure 8 is
920 displayed with gray bars. All colored bars except for the blue bars (UKMO) represent the
921 hindcast skill obtained over 1990-2012, for which the statistical model was re-built. The
922 hindcast skill of the UKMO system was computed over 1993-2016. Black dots indicate the
923 skill obtained over longer hindcast periods (see Table 1). The crosses overlayed with the blue
924 bars indicate the skill with an increased ensemble size by using up to 17-day lags (compared

925 to 7-member burst ensemble used for the skill shown with the blue bars). (b,c) Dynamical
926 and statistical forecasts of standardized SPVI for 2019 and 2002, respectively. The observed
927 anomalies are displayed with light blue bars. All the forecast anomalies were computed with
928 each system's climatological mean and standard deviation from its hindcast periods. The
929 abscissa labels show the forecast initialization dates. Displayed dynamical forecasts are the
930 ensemble mean forecasts (except for NASA forecasts), and details of the forecast systems and
931 ensemble sizes are provided in Table 1.

932

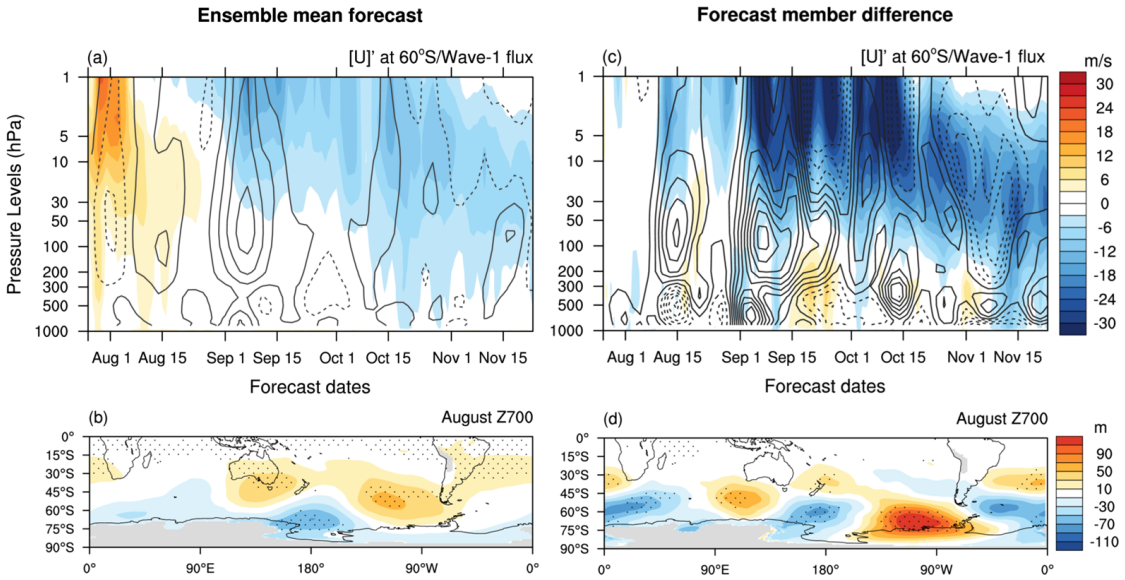

FIG 10. (Left panels) 11-member ensemble mean forecasts of (a) daily [U]' at 60°S (color shading) overlayed with standardized upward wave-1 activity flux ($F_{(p)}$'; contours) and (b) August mean Z700 anomalies (color shading) from the BoM system. Forecasts were initialized on 25 July 2019. In (a) the solid (dashed) thick contour indicates the poleward (equatorward) heat flux and so upward (downward) wave propagation. Normalization of the wave activity flux by its standard deviation was done at each vertical level. Stippling in (b) indicates anomalies at the ±5% tails of the climatological distribution of BoM hindcasts. (Right panels) (c), (d) Same as in (a) and (b), respectively, except the mean differences between the three forecast members of the weakest spring polar vortex and those of the strongest spring polar vortex. The color shading interval is 3 ms^{-1}, and the contour interval is 1σ starting from -11.5σ in (a) and (c). The color shading interval is 20 m in (b) and (d). Stippling in (d) indicates statistical significance on the difference of the two means at the 10% level, assessed by a two-tailed Student t-test with the sample size of three in each group.

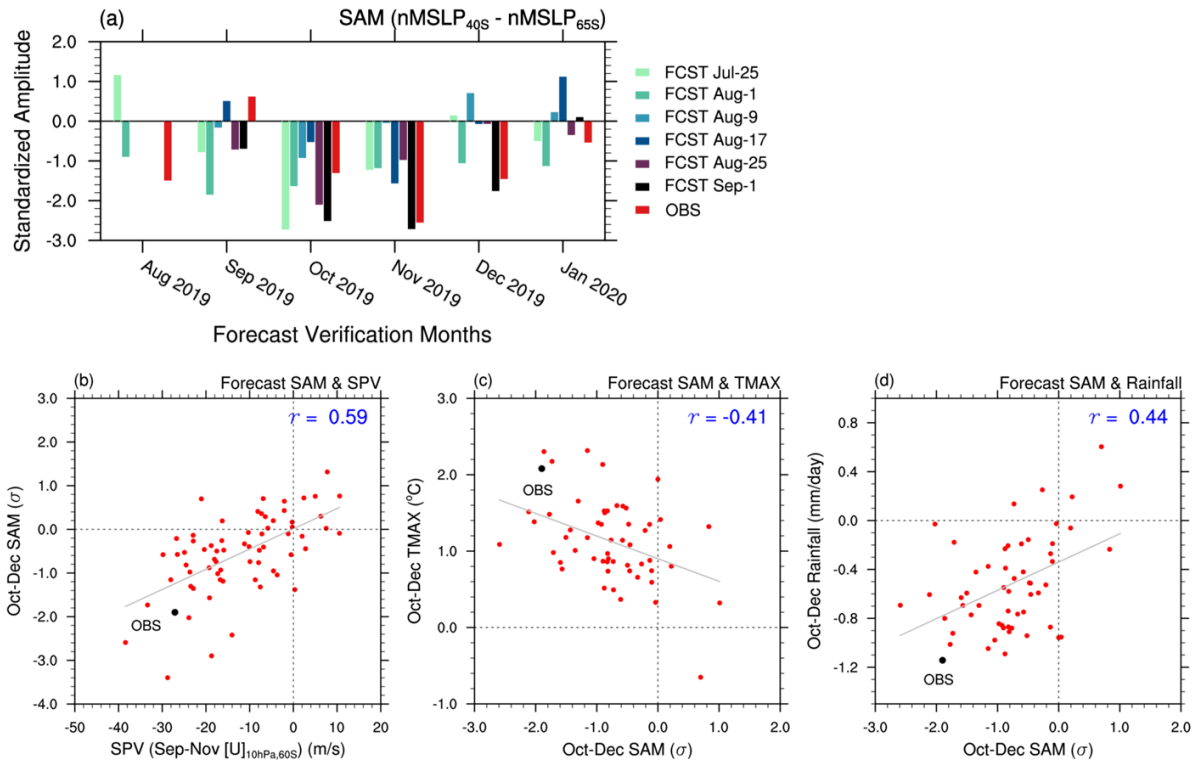

949

950 **FIG 11.** (a) BoM 11-member ensemble mean forecasts of monthly SAM initialized on 25
951 July, 1, 9, 17, 25 August and 1 September of 2019. The forecast SAM values were computed
952 by the normalized MSLP difference between 40°S and 65°S following Gong and Wang
953 (1999)'s definition. The red color bars indicate the observed SAM values obtained from the
954 British Antarctic Survey (http://www.nerc-bas.ac.uk/icd/gjma/sam.html), which was
955 computed in the same way as Gong and Wang (1999)'s method but with station data
956 (Marshall 2003). (b) 66 ensemble member forecasts (red dots) initialized on the dates shown
957 in (a) for the SPVI and OND mean SAM. The observed values are displayed with the black
958 dot. (c),(d) Relationship of the SAM with eastern Australian Tmax and rainfall (east of
959 140°E, 10-45°S), respectively, in 55 forecasts (11 members initialised on 25 August, 1, 9, 17,
960 25 September of 2019) for the OND season.

961

Operational Centers	Prediction Systems	Atmospheric resolution	Available full length of hindcast period	Hindcast Ensemble size per initialization date	2002/2019 forecast ensemble size per initialization date
BoM	ACCESS-S1	N216 L85	1990-2012	11	11
ECMWF	SEAS5	TCo319 (36km) L91	1981-2019	25 (Jul, Sep) and 51 Aug	2002: 25 (Jul, Sep) 51 (Aug) 2019: 51
JMA	JMA/MRI-CPS2	TL159 L60	1981-2014	5	2002: 5 2019: 13
NASA	GEOS-S2S-2	0.5° lat/lon L72	1981-2019	1	1
UKMO	GloSea5	N216 L85	1993-2016	7	2002: 7 2019: 8§

962

963 **Table 1**: Details of the five operational dynamical forecast systems and their forecasts used in
964 this study. The UKMO forecast skill indicated by the crosses overlayed with the blue bars in
965 FIG. 9a was computed with the ensemble mean of 21-member forecasts formed with time
966 lags. § denotes the ensemble formation with 2 burst members over 4 consecutive days.